THE ASTROPHYSICAL JOURNAL, 484:256–276, 1997 July 20

NEW PROTOSTELLAR COLLAPSE CANDIDATES: AN HCO^+ SURVEY OF THE CLASS 0 SOURCES

ERIK M. GREGERSEN[1] AND NEAL J. EVANS II[2]
Department of Astronomy, University of Texas at Austin, Austin, TX 78712-1083
SHUDONG ZHOU[3]
Department of Astronomy, University of Illinois, Urbana, IL 61801
AND
MINHO CHOI[4]
Institute of Astronomy and Astrophysics, Academia Sinica, P.O. Box 1-87, Nankang, Taiwan 115, Republic of China
Received 1996 March 21; accepted 1997 February 18

ABSTRACT

We have observed 23 class 0 sources in the HCO^+ $J = 4$–3 and 3–2 lines. The mean bolometric temperature of the 16 sources with well-determined values is 44 K, and the mean luminosity is 5.7 $L_\odot$, excluding two sources of considerably higher luminosity. Nine sources, including three sources previously suggested to be collapsing, have the correct (blue) spectral line asymmetry for infall in both lines. Three sources have the opposite (red) asymmetry in both lines, and one source, L1157, has a red asymmetry in HCO^+ $J = 4$–3 and a blue asymmetry in $J = 3$–2. The rest have no significant or consistent asymmetry. The $H^{13}CO^+$ $J = 4$–3 and 3–2 lines were also observed to find the velocity of the ambient gas, and sources with an interesting line asymmetry were mapped. A Monte Carlo code was used to produce an evolutionary sequence of collapsing cloud models of the HCO^+ $J = 4$–3 and 3–2 lines and to compare various diagnostics of the resulting line profiles. The same code was used to compare infall models to the observations in one source, L1527. The results were consistent with previous collapse models. Based on integrated intensity maps of the line peaks and wings, as well as the velocity of the $H^{13}CO^+$ line, we select six of the nine sources with a blue line asymmetry as good *candidates* for protostellar collapse. Further evidence is needed to establish that infall is taking place. The HCO^+ spectra are not conclusive because bipolar outflows produce strong emission, which can confuse the issue in any individual source. However, the predominance of blue asymmetries over red asymmetries is not naturally explained in outflow models, whereas it is expected in collapse models.

Subject headings: ISM: jets and outflows — ISM: molecules — ISM: structure — stars: formation

1. INTRODUCTION

An important aim of the study of young stellar objects (YSOs) has been to classify them in an evolutionary sequence and identify when in this sequence protostellar collapse occurs. The most widely used classification scheme is that of Lada & Wilking (1984) and Lada (1987), which divides YSOs into three categories based on the slope of their infrared spectral energy distribution (SED). The oldest population, class III, have a blackbody-like SED and are interpreted as pre–main-sequence stars without a disk. Class II sources have a flat or negatively sloped SED in the infrared and are understood as classical T Tauri stars with an optically thick disk of circumstellar dust. Class I sources have an SED that rises with wavelength up to 100 μm and are believed to be collapsing protostars (Adams, Lada, & Shu 1987; Wilking, Lada, & Young 1989a).

Recently, André, Ward-Thompson, & Barsony (1993, hereafter AWB) noted that several sources have not been detected in the near-infrared and have blackbody-like SEDs that peak in the submillimeter, suggesting extremely low dust temperatures ($T_D \sim 20$ K). They called these sources class 0 (which they defined as a submillimeter source with $L_{\rm bol}/L_{1.3\ {\rm mm}} \lesssim 2 \times 10^4$) because their cold temperature suggested an object even younger than typical class I objects. Barsony (1994) listed the following as characteristics of these sources in addition to the low $L_{\rm bol}/L_{1.3\ {\rm mm}}$: an SED like a 30 K blackbody, undetected at $\lambda < 10$ μm, and a molecular outflow. Chen et al. (1995) found that class 0 sources have bolometric temperatures ($T_{\rm bol}$) less than 70 K. $T_{\rm bol}$ is the temperature of a blackbody with the same mean frequency as the SED of the source (Myers & Ladd 1993).

André & Montmerle (1994) argued that class 0 sources have more circumstellar mass than stellar mass. They suggested that class 0 sources are still in their active accretion phase, while class I sources have already accreted most of their mass. If this suggestion is correct, class 0 sources should be good candidates to show kinematic evidence of collapse.

The goal of this project was to survey all the class 0 objects that had been cited in the astronomical literature for signs of protostellar collapse. Since we were unable to determine if every claimed class 0 object meets the criterion of AWB or Barsony, the selected sample of 23 sources (see Table 1) includes any source that has been identified as either a definite or a probable class 0 source. Although this criterion is rather loose, we have checked the credentials of our sources by computing $T_{\rm bol}$, using the procedure of Myers & Ladd (1993), for all sources with sufficient data. Since many of these sources have few spectral data points, we relaxed one criterion of Myers & Ladd. They required six spectral data points, but we used as few as four, which seemed to be adequate as long as the photometric data lay

[1] erik@astro.as.utexas.edu.
[2] nje@astro.as.utexas.edu.
[3] zhou@astro.uiuc.edu.
[4] minho@biaa3.biaa.sinica.edu.tw.

TABLE 1

LIST OF CLASS 0 SOURCES

Name	R.A. (1950.0)	Decl. (1950.0)	Off Position (arcsec)	Reference
L1448-N	03 22 31.5	30 34 49.0	(−1200, 0)	1
L1448-C	03 22 34.4	30 33 35.0	(−1200, 0)	1
NGC 1333 IRAS 4A	03 26 04.78	31 03 13.6	(150, 120)	2
NGC 1333 IRAS 4B	03 26 06.48	31 02 50.8	(150, 120)	2
L1551-NE	04 28 50.5	18 02 10.0	(−600, 0)	3
L1527	04 36 49.3	25 57 16.0	(−600, 0)	4
RNO 43MM	05 29 30.6	12 47 35.0	(−900, 0)	5
NGC 2024 FIR 5	05 39 13.0	−01 57 08.0	(−1800, 0)	6
NGC 2024 FIR 6	05 39 13.7	−01 57 30.0	(−1800, 0)	6
HH 25MMS	05 43 34.0	−00 14 42.0	(−900, 0)	7
IRAS 08076	08 07 40.2	−35 56 07.0	(−900, 0)	8
VLA 1623	16 23 24.9	−24 17 46.3	(0, −900)	9
IRAS 16293	16 29 20.9	−24 22 13.0	(0, −900)	10
L483	18 14 50.6	−04 40 49.0	(−600, 0)	11
Serpens SMM1	18 27 17.3	01 13 23.0	(−900, 0)	12
Serpens SMM4	18 27 24.7	01 11 10.0	(−900, 0)	12
Serpens SMM3	18 27 27.3	01 11 55.0	(−900, 0)	12
Serpens SMM2	18 27 28.0	01 10 45.0	(−900, 0)	12
L723	19 15 42.0	19 06 49.0	(−900, 0)	13
B335	19 34 35.4	07 27 24.0	(−600, 0)	14
IRAS 20050	20 05 02.5	27 20 09.0	(−900, 0)	15
S106FIR	20 25 32.44	37 12 48.0	(−900, 0)	16
L1157	20 38 39.6	67 51 33.0	(−900, 0)	17

NOTE.—Units of right ascension are hours, minutes, and seconds, and units of declination are degrees, arcminutes, and arcseconds.

REFERENCES.—(1) Curiel et al. 1990; (2) Sandell et al. 1991; (3) Moriarty-Schieven et al. 1995a; (4) Zhou et al. 1994; (5) Zinnecker et al. 1992; (6) Mezger et al. 1992; (7) Bontemps et al. 1995; (8) Persi et al. 1990; (9) André & Montmerle 1994; (10) Walker et al. 1986; (11) Mardones et al. 1994; (12) Casali et al. 1993; (13) Davidson 1987; (14) Chandler & Sargent 1993; (15) Bachiller et al. 1995; (16) Richer et al. 1993; (17) Tafalla & Bachiller 1995.

TABLE 2

BOLOMETRIC TEMPERATURE OF CLASS 0 SOURCES

Source	Range (μm)	T_{bol} (K)	Distance (pc)	L_{bol} ($L_\odot$)	Reference
L1448-C	12–3500	55 ± 9	300	6 ± 0.4	1
NGC 1333 IRAS 4A	50–2000	34 ± 2	350	9.5 ± 0.3	2, 3
NGC 1333 IRAS 4B	50–2000	36 ± 2	350	8.4 ± 0.9	2, 3
L1551-NE	12–1260	75 ± 18	140	3.9 ± 0.5	4, 5
L1527	25–800	41 ± 6	140	1.3 ± 0.1	6, 7
RNO 43MM	60–1300	36 ± 4	400	4.5 ± 0.3	6, 8
IRAS 08076	12–1300	74 ± 15	400	8.9 ± 0.3	6, 9
IRAS 16293	25–3000	42 ± 0.7	125	11 ± 0.1	6, 10, 11
L483	25–450	48 ± 5	200	9.5 ± 0.5	6, 12
Serpens SMM1	20–2000	45 ± 5	310	45 ± 3	13, 14, 15
Serpens SMM4	800–2000	35 ± 5	310	3.9 ± 0.3	13, 14, 15
Serpens SMM3	60–1300	38 ± 5	310	4.5 ± 0.4	13, 14, 15
Serpens SMM2	60–1100	38 ± 5	310	2.7 ± 0.2	13, 14, 15
L723	25–1300	39 ± 4	300	2.8 ± 0.2	6, 16, 17
B335	60–1300	29 ± 3	250	2.5 ± 0.2	6, 16, 18, 19, 20, 21
IRAS 20050	12–2700	69 ± 7	700	206 ± 13	6, 22
VLA 1623	350–2000	$\gtrsim 8.3 \pm 1.9$	125	$\gtrsim 0.06 \pm 0.009$	11, 23
L1157	25–100	$\lesssim 44 \pm 9$	440	$\gtrsim 6 \pm 0.6$	6
L1448-N	12–100	…	300	…	6
NGC 2024 FIR 5	350–2700	…	415	…	24, 25, 26
NGC 2024 FIR 6	870–2700	…	415	…	24, 25, 26
HH 25MMS	52–1300	…	400	…	27, 28
S106FIR	450–1100	…	600	…	29

REFERENCES.—(1) Bachiller, André, & Cabrit 1991; (2) Sandell et al. 1991; (3) Jennings et al. 1987; (4) Emerson et al. 1984; (5) Barsony & Chandler 1993; (6) IRAS Point Source Catalog; (7) Ladd et al. 1991; (8) Zinnecker et al. 1992; (9) Persi et al. 1994; (10) Walker, Adams, & Lada 1990; (11) André et al. 1990b; (12) Fuller et al. 1995; (13) McMullin et al. 1994; (14) Casali et al. 1993; (15) Hurt & Barsony 1996; (16) Davidson 1987; (17) Cabrit & André 1991; (18) Chandler et al. 1990; (19) Gee et al. 1985; (20) Keene et al. 1983; (21) Chandler & Sargent 1993; (22) Wilking et al. 1989b; (23) André et al. 1993; (24) Mezger et al. 1988; (25) Mezger et al. 1992; (26) Wilson, Mehringer, & Dickel 1995; (27) Cohen et al. 1984; (28) Bontemps et al. 1995; (29) Richer et al. 1993.

TABLE 3

LIST OF OBSERVED LINES

Molecule	Transition	Beamwidth (arcsec)	η_{mb}	δv (km)	Frequency (GHz)
$HC^{18}O^+$	$J = 3–2$	27	0.66	0.17	255.479389
$H^{13}CO^+$	$J = 3–2$	26	0.66	0.17	260.255478
HCO^+	$J = 3–2$	26	0.66	0.16	267.557620
$H^{13}CO^+$	$J = 4–3$	20	0.62	0.13	346.998540
HCO^+	$J = 4–3$	20	0.62	0.12	356.734288

on either side of the peak of the SED. The values of T_{bol} are given in Table 2, along with information on L_{bol}, distance, and references. All 16 of the sources for which T_{bol} can be calculated lie in the class 0 category ($T_{bol} < 70$ K) within error bars. The mean T_{bol} is 44 K and the mean L_{bol} is 5.7 $L_\odot$, excluding the extremely luminous sources IRAS 20050 and SMM1. This sample is primarily one of very embedded, low-luminosity objects. For two other sources, there are enough photometric data to calculate upper limits (if data are available on the blue side of the peak) or lower limits (if data are available on the red side of the peak) for T_{bol}. Some of the sources without sufficient data to compute T_{bol} or L_{bol} lie in regions of considerably higher luminosity, where confusion prevents separation of the contributions of different sources in the far-infrared.

The method of spectral line asymmetry (Leung & Brown 1977; Zhou 1992) was used to identify collapse candidates. An optically thick line in a collapsing core shows a blue asymmetry in the line profile toward the collapse center, while an optically thin line appears symmetric. The optically thick lines we used were the $J = 4–3$ and 3–2 transitions of HCO^+, and the optically thin lines were those of rarer isotopomers of HCO^+, like $H^{13}CO^+$ and $HC^{18}O^+$. Clumpy outflows can also produce peaks that may be either red or blue; we address the possible confusion between infall and outflow in § 4.3.

2. OBSERVATIONS AND RESULTS

Observations were made of 23 class 0 sources at the 10.4 m telescope of the Caltech Submillimeter Observatory (CSO)[5] at Mauna Kea, Hawaii, in 1994 October, 1994 November, 1994 December, 1995 March, 1995 June, 1995 December, and 1996 June. The sources are listed in Table 1 with their celestial coordinates and the off position used for position switching. The off positions were checked for absence of detectable HCO^+ emission. We used SIS receivers operating at 230 and 345 GHz, and the back end was a 1024 channel, acousto-optic spectrometer with a bandwidth of 49.5 MHz. The frequency resolution varied over the five runs from about 2.5 to 3 channels, which corresponds to a velocity resolution of 0.14–0.17 km s^{-1} at 260 GHz and of 0.10–0.12 km s^{-1} at 357 GHz. Chopper-wheel calibration was used to obtain the antenna temperature, T_A^*. The lines we observed and their frequencies are listed in Table 3 along with the main beam efficiency, the velocity resolution, and the beam size at each frequency. The efficiencies were calculated from numerous observations of planets. Data from separate runs were resampled to the resolution of the run with the worst frequency resolution before averaging. A first-order baseline was removed before scans were averaged. Seven sources that had noticeable asymmetry (either to the blue or red side) at the central position were mapped (map sizes ranged from $30'' \times 30''$ to $60'' \times 90''$) and observed in at least one transition of $H^{13}CO^+$.

Twenty-three sources were observed in this survey. All 23 sources were observed in the HCO^+ $J = 3–2$ line. Eighteen sources were observed in the HCO^+ $J = 4–3$ line. Nineteen and four sources were observed in the $H^{13}CO^+$ $J = 3–2$ and 4–3 lines, respectively. Seven sources were observed in the $J = 3–2$ line of $HC^{18}O^+$.

Nine sources showed blue asymmetry in both the HCO^+ $J = 4–3$ and 3–2 lines. Three sources had a red asymmetry in both lines, and one source, L1157, had opposite asymmetry in each of the two lines. Five sources showed no asymmetry in both lines. Five other sources were observed only in the $J = 3–2$ line. Of the five sources observed only in the $J = 3–2$ line, three showed no asymmetry, one showed a red asymmetry, and one showed a blue asymmetry.

The line properties are listed in Table 4. T_A^* is the highest temperature in the line profile. For singly peaked lines, the velocity and ΔV are the centroid and width of the line, found by fitting a single Gaussian to the line profile. For lines that have two peaks, we list two values of T_A^* and velocity, one for each peak, and we give one value for the line width, which is the full width across the spectrum at the temperature where the weaker peak falls to half power.

3. INDIVIDUAL SOURCES

3.1. *L1448-N*

This core in Perseus ($d = 300$ pc) is coincident with IRS 3 and lies in the outflow lobe of L1448-C. An H_2O maser coincides with the peak of the ammonia emission (Anglada et al. 1989). Bachiller et al. (1990) mapped the outflow in CO and found it to be quite weak and not well collimated. A clear red asymmetry is seen in HCO^+ $J = 3–2$ (Fig. 5).

3.2. *L1448-C*

Bachiller et al. (1990) discovered this highly collimated outflow ($d = 300$ pc), which had no known exciting source. Curiel et al. (1990) found a radio continuum source at the center of the outflow. Line asymmetries consistent with infall have been seen in the 85 GHz line of C_3H_2 (Mardones et al. 1994). The HCO^+ $J = 4–3$ and 3–2 lines display an asymmetry with the red peak stronger than the blue peak. The $H^{13}CO^+$ $J = 3–2$ line peaks on the red side of the self-absorption dip, but the $H^{13}CO^+$ $J = 4–3$ line peaks on the red peak of the HCO^+ $J = 4–3$ line (Figs. 3 and 4), suggesting that the blue peak is an optically thin clump of outflowing gas. In support of this interpretation, we note that the velocity of the blue peak in the HCO^+ spectrum is well outside the line profile seen in C_3H_2 by Mardones et al. Consequently, our data do not provide evidence for or against the suggestion by Mardones et al. that L1448-C may be collapsing.

3.3. *NGC 1333 IRAS 4A*

Jennings et al. (1987) discovered NGC 1333 IRAS 4 ($d = 350$ pc) in IRAS CPC observations. Submillimeter and millimeter photometry by Sandell et al. (1991) revealed a double source (IRAS 4A and 4B) with a $31''$ separation and a SED that peaks at about 500 μm. Recent interferometer observations have shown that IRAS 4A is itself a binary with a separation of $1''.8$ (Lay, Carlstrom, & Hills 1995). Our

[5] The CSO is operated by the California Institute of Technology under funding from the National Science Foundation, contract AST 90-15755.

TABLE 4

RESULTS

Source	Molecule	Line	T_A^* (K)	Velocity (km s^{-1})	ΔV (km s^{-1})
L1448-N	HCO^+	$J = 3–2$	4.02 ± 0.04	5.02 ± 0.01	2.07 ± 0.01
	$H^{13}CO^+$	$J = 3–2$	1.16 ± 0.06	4.86 ± 0.02	1.63 ± 0.05
L1448-C	HCO^+	$J = 4–3$	1.26 ± 0.10	4.38 ± 0.07	2.02 ± 0.13
	...	...	2.69 ± 0.10	5.59 ± 0.07	...
	...	$J = 3–2$	1.65 ± 0.06	4.31 ± 0.09	2.21 ± 0.17
	...	...	2.75 ± 0.06	5.67 ± 0.09	...
	$H^{13}CO^+$	$J = 4–3$	0.69 ± 0.06	5.45 ± 0.02	0.78 ± 0.05
	...	$J = 3–2$	0.99 ± 0.02	5.31 ± 0.01	0.83 ± 0.02
NGC 1333 IRAS 4A	HCO^+	$J = 4–3$	4.23 ± 0.07	6.61 ± 0.07	3.36 ± 0.13
	...	...	1.03 ± 0.07	8.22 ± 0.07	...
	...	$J = 3–2$	5.15 ± 0.03	6.47 ± 0.09	3.91 ± 0.17
	...	...	1.24 ± 0.03	8.17 ± 0.09	...
	$H^{13}CO^+$	$J = 4–3$	0.49 ± 0.05	6.99 ± 0.03	1.25 ± 0.08
	...	$J = 3–2$	0.73 ± 0.05	7.06 ± 0.02	1.21 ± 0.06
NGC 1333 IRAS 4B	HCO^+	$J = 4–3$	3.08 ± 0.07	6.61 ± 0.07	3.23 ± 0.13
	...	...	0.91 ± 0.07	7.96 ± 0.07	...
	...	$J = 3–2$	3.73 ± 0.09	6.47 ± 0.09	3.40 ± 0.17
	...	...	0.88 ± 0.09	8.00 ± 0.09	...
	$H^{13}CO^+$	$J = 4–3$	<0.08	...	...
		$J = 3–2$	0.33 ± 0.04	7.14 ± 0.05	1.21 ± 0.13
L1551-NE	HCO^+	$J = 3–2$	1.95 ± 0.05	6.27 ± 0.08	2.73 ± 0.16
	...	...	0.93 ± 0.05	7.24 ± 0.08	...
	...	...	0.82 ± 0.05	8.04 ± 0.08	...
	$H^{13}CO^+$	$J = 3–2$	0.21 ± 0.03	7.23 ± 0.08	1.60 ± 0.16
L1527	HCO^+	$J = 4–3$	4.33 ± 0.04	5.70 ± 0.07	2.16 ± 0.13
	...	...	1.81 ± 0.04	6.50 ± 0.07	...
	...	$J = 3–2$	5.00 ± 0.04	5.51 ± 0.09	2.38 ± 0.17
	...	...	2.47 ± 0.04	6.36 ± 0.09	...
	$H^{13}CO^+$	$J = 4–3$	0.35 ± 0.03	6.01 ± 0.02	0.69 ± 0.06
		$J = 3–2$	0.75 ± 0.03	5.94 ± 0.01	0.93 ± 0.03
	$HC^{18}O^+$	$J = 4–3$	<0.07	...	...
RNO 43MM	HCO^+	$J = 3–2$	2.54 ± 0.09	10.37 ± 0.01	1.08 ± 0.16
NGC 2024 FIR 5	HCO^+	$J = 3–2$	8.22 ± 0.08	11.74 ± 0.01	1.70 ± 0.16
	$H^{13}CO^+$	$J = 3–2$	2.08 ± 0.07	11.38 ± 0.01	1.84 ± 0.04
NGC 2024 FIR 6	HCO^+	$J = 3–2$	7.78 ± 0.09	11.73 ± 0.01	2.32 ± 0.16
	$H^{13}CO^+$	$J = 3–2$	1.58 ± 0.07	11.25 ± 0.02	2.18 ± 0.05
HH 25MMS	HCO^+	$J = 4–3$	2.02 ± 0.03	9.83 ± 0.07	2.13 ± 0.13
	...	...	1.56 ± 0.03	10.90 ± 0.07	...
		$J = 3–2$	3.53 ± 0.05	10.02 ± 0.01	2.21 ± 0.01
	$H^{13}CO^+$	$J = 3–2$	0.84 ± 0.05	10.34 ± 0.02	1.19 ± 0.05
IRAS 08076	HCO^+	$J = 4–3$	1.95 ± 0.06	6.28 ± 0.01	1.60 ± 0.13
	...	$J = 3–2$	4.53 ± 0.12	6.19 ± 0.01	1.19 ± 0.17
	$H^{13}CO^+$	$J = 3–2$	1.22 ± 0.06	6.48 ± 0.01	0.91 ± 0.03
VLA 1623	HCO^+	$J = 4–3$	2.01 ± 0.10	2.31 ± 0.06	3.26 ± 0.12
	...	...	4.39 ± 0.10	3.40 ± 0.06	...
	...	...	4.62 ± 0.10	4.24 ± 0.06	...
	...	$J = 3–2$	3.42 ± 0.06	2.19 ± 0.08	2.89 ± 0.16
	...	...	3.96 ± 0.06	3.32 ± 0.08	...
	...	...	4.36 ± 0.06	4.28 ± 0.08	...
	$H^{13}CO^+$	$J = 3–2$	1.10 ± 0.05	3.98 ± 0.01	1.03 ± 0.03
IRAS 16293	HCO^+	$J = 4–3$	15.09 ± 0.14	3.48 ± 0.06	4.10 ± 0.12
	...	...	4.76 ± 0.14	4.86 ± 0.06	...
	...	$J = 3–2$	17.60 ± 0.07	3.31 ± 0.08	3.37 ± 0.16
	...	...	6.66 ± 0.07	4.92 ± 0.08	...
	$H^{13}CO^+$	$J = 3–2$	1.52 ± 0.07	3.65 ± 0.17	2.48 ± 0.34
	...	...	1.33 ± 0.07	4.81 ± 0.17	...
	$HC^{18}O^+$	$J = 3–2$	0.18 ± 0.05	4.52 ± 0.08	2.70 ± 0.31
L483	HCO^+	$J = 4–3$	1.12 ± 0.13	4.87 ± 0.06	2.65 ± 0.12
	...	...	3.48 ± 0.13	5.71 ± 0.06	...
	...	$J = 3–2$	1.47 ± 0.04	4.77 ± 0.08	2.33 ± 0.16
	...	...	3.10 ± 0.04	5.86 ± 0.08	...
	$H^{13}CO^+$	$J = 3–2$	0.97 ± 0.04	5.57 ± 0.01	0.90 ± 0.03
	$HC^{18}O^+$	$J = 3–2$	0.11 ± 0.01	5.31 ± 0.06	1.08 ± 0.23
Serpens SMM1	HCO^+	$J = 4–3$	2.14 ± 0.14	7.13 ± 0.06	3.87 ± 0.12
	...	...	2.17 ± 0.14	9.79 ± 0.06	...
	...	$J = 3–2$	2.30 ± 0.12	7.26 ± 0.08	4.19 ± 0.15
	...	...	2.40 ± 0.12	9.74 ± 0.08	...
	$H^{13}CO^+$	$J = 3–2$	1.19 ± 0.06	8.53 ± 0.02	1.55 ± 0.04
	$HC^{18}O^+$	$J = 3–2$	0.24 ± 0.02	8.44 ± 0.04	1.47 ± 0.11

TABLE 4—*Continued*

Source	Molecule	Line	T_A^* (K)	Velocity (km s^{-1})	ΔV (km s^{-1})
Serpens SMM4.....	HCO^+	$J = 4–3$	4.56 ± 0.08	7.66 ± 0.06	3.98 ± 0.12
	...	...	1.73 ± 0.08	9.10 ± 0.06	...
	...	$J = 3–2$	6.58 ± 0.04	7.24 ± 0.08	6.58 ± 0.16
	...	...	2.16 ± 0.04	9.41 ± 0.08	...
	$H^{13}CO^+$	$J = 3–2$	0.95 ± 0.04	8.02 ± 0.02	1.56 ± 0.05
	$HC^{18}O^+$	$J = 3–2$	0.15 ± 0.02	7.65 ± 0.04	0.92 ± 0.10
Serpens SMM3.....	HCO^+	$J = 4–3$	3.02 ± 0.16	7.83 ± 0.02	1.45 ± 0.12
	...	$J = 3–2$	5.00 ± 0.06	7.74 ± 0.01	1.46 ± 0.11
Serpens SMM2.....	HCO^+	$J = 4–3$	1.68 ± 0.08	6.93 ± 0.06	2.53 ± 0.12
	...	...	1.06 ± 0.08	8.02 ± 0.06	...
	...	$J = 3–2$	2.75 ± 0.05	6.66 ± 0.06	2.81 ± 0.11
	...	...	2.37 ± 0.05	7.89 ± 0.06	...
	$H^{13}CO^+$	$J = 3–2$	0.55 ± 0.03	7.08 ± 0.08	1.82 ± 0.16
	...	...	0.32 ± 0.03	8.23 ± 0.08	...
	$HC^{18}O^+$	$J = 3–2$	0.07 ± 0.02	6.62 ± 0.08	0.81 ± 0.15
L723.....	HCO^+	$J = 4–3$	1.09 ± 0.15	11.02 ± 0.05	1.56 ± 0.12
	...	$J = 3–2$	1.79 ± 0.05	11.06 ± 0.01	1.93 ± 0.16
B335.....	HCO^+	$J = 4–3$	2.37 ± 0.07	8.17 ± 0.06	1.69 ± 0.12
	...	...	1.05 ± 0.07	8.78 ± 0.06	...
	...	$J = 3–2$	3.31 ± 0.06	8.00 ± 0.08	1.39 ± 0.16
	...	...	1.59 ± 0.06	8.78 ± 0.08	...
	$H^{13}CO^+$	$J = 3–2$	0.91 ± 0.07	8.41 ± 0.02	0.62 ± 0.04
	$HC^{18}O^+$	$J = 3–2$	0.09 ± 0.02	8.25 ± 0.04	0.60 ± 0.11
IRAS 20050.....	HCO^+	$J = 4–3$	3.12 ± 0.08	5.93 ± 0.01	2.89 ± 0.12
	...	$J = 3–2$	3.26 ± 0.08	5.27 ± 0.05	4.51 ± 0.11
	...	...	2.32 ± 0.08	7.30 ± 0.05	...
	$H^{13}CO^+$	$J = 3–2$	0.42 ± 0.05	6.09 ± 0.06	2.56 ± 0.14
S106FIR	HCO^+	$J = 4–3$	4.55 ± 0.16	-1.07 ± 0.02	3.50 ± 0.12
	...	$J = 3–2$	4.14 ± 0.11	-1.27 ± 0.02	3.22 ± 0.16
L1157	HCO^+	$J = 4–3$	1.17 ± 0.08	2.34 ± 0.06	1.69 ± 0.12
	...	...	1.51 ± 0.08	3.18 ± 0.06	...
	...	$J = 3–2$	2.03 ± 0.08	2.25 ± 0.08	1.93 ± 0.16
	...	...	1.78 ± 0.08	3.22 ± 0.08	...
	$H^{13}CO^+$	$J = 3–2$	0.31 ± 0.07	2.83 ± 0.09	1.52 ± 0.20

HCO^+ $J = 4–3$ and 3–2 data show a blue asymmetry, with the $H^{13}CO^+$ $J = 3–2$ line slightly offset to the blue from the self-absorption dip (Fig. 1).

3.4. *NGC 1333 IRAS 4B*

This source ($d = 350$ pc) appears to be a system of more than two stars (Lay et al. 1995). A strong blue asymmetry is seen in the HCO^+ $J = 3–2$ line (Fig. 1). The red peak is very weak in the HCO^+ $J = 4–3$ line (Fig. 2). The slight blue offset of the $H^{13}CO^+$ $J = 3–2$ line from the absorption dip that was seen in IRAS 4A is also present here.

3.5. *L1551-NE*

This source ($d = 140$ pc) lies in a lobe of the famous L1551 outflow. Moriarty-Schieven et al. (1995a) identified this as an object between class I and class 0; we find a T_{bol} of 75 ± 18 K. CS $J = 3–2$ and $J = 5–4$ observations show a blue asymmetric line profile (Moriarty-Schieven et al. 1995b). Our HCO^+ $J = 3–2$ observations show a multi-peaked line profile (Fig. 5). The blue peak in our HCO^+ $J = 3–2$ spectrum has the same velocity as that observed in the double-peaked CS spectra of Moriarty-Schieven et al. (1995b). The $H^{13}CO^+$ $J = 3–2$ line has two peaks, and the HCO^+ $J = 3–2$ has three. The spectrum is too complex to decide whether collapse is occurring.

3.6. *L1527*

The spectral energy distribution of this source ($d = 140$ pc) is quite similar to those of B335 and L483 (Ladd et al. 1991). Zhou et al. (1994), Mardones et al. (1994), and Myers et al. (1995) have presented observations that show infall asymmetry in the H_2CO $J = 3_{12}–2_{11}$ line, the 85 GHz line of C_3H_2, and the H_2CO $J = 2_{12}–1_{11}$ line, respectively. Our HCO^+ $J = 4–3$ and 3–2 data also show a prominent infall signature. The $H^{13}CO^+$ $J = 4–3$ and $J = 3–2$ lines peak in the self-absorption dips of the HCO^+ $J = 4–3$ and 3–2 line profiles (Figs. 1 and 2).

3.7. *RNO 43MM*

No emission has been detected from this source ($d = 400$ pc) at 12 or 25 μm (IRAS Point Source Catalog), and its spectral energy distribution peaks at about 100 μm (Zinnecker et al. 1992). The derived T_{bol} of 36 K confirms that it is a class 0 source. Our HCO^+ $J = 3–2$ data show a symmetric line (Fig. 5).

3.8. *NGC 2024 FIR 5*

These two sources (FIR 5 and FIR 6) ($d = 415$ pc) were found by Mezger et al. (1988), who suggested that they were isothermal protostars. A unipolar jet has been seen near this source, but the identification of FIR 5 as the driving source is uncertain (Richer, Hills, & Padman 1992). The identification of FIR 5 and FIR 6 as isothermal protostellar condensations is controversial because warm gas is present in these cores, suggesting that the objects may be more evolved than Mezger et al. (1988) believed (Lis, Carlstrom, & Phillips 1991). CS observations suggest that these two sources are massive enough to form stars (Chandler & Carlstrom 1996). No collapse asymmetry is seen in the HCO^+ $J = 3–2$ line, but a low-velocity shoulder was detected (Fig. 5).

3.9. *NGC 2024 FIR 6*

A bipolar outflow with a very young dynamical time scale (<400 yr) is present (Richer 1990). An H_2O maser is

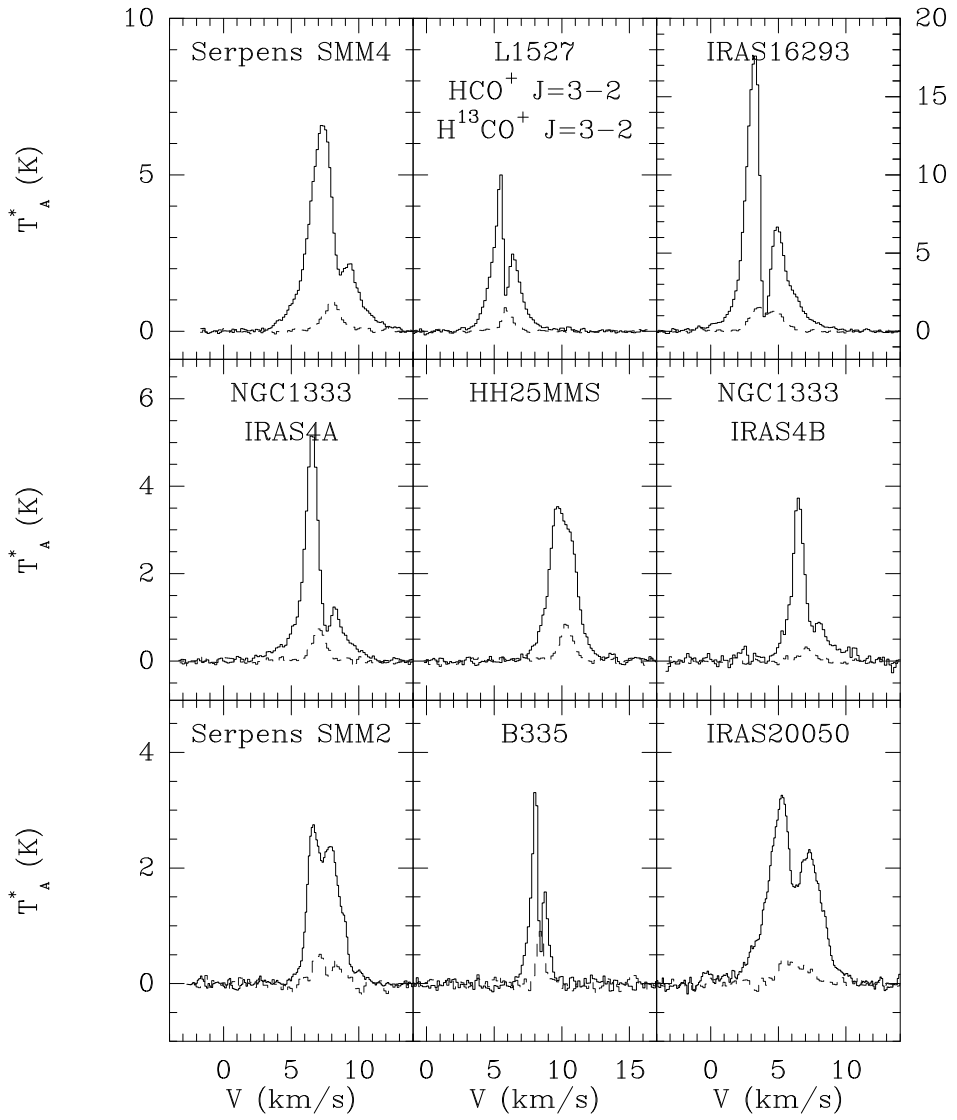

FIG. 1.—HCO^+ and $H^{13}CO^+$ $J = 3$–2 spectra toward the center of nine class 0 sources. These sources all show a blue asymmetry in the HCO^+ $J = 3$–2 line characteristic of collapse. The solid line is the HCO^+ spectrum, and the dashed line is the $H^{13}CO^+$ spectrum. The scale for the spectra of IRAS 16293 is shown on the right-hand side of its panel. The $H^{13}CO^+$ $J = 3$–2 spectrum for HH 25MMS is from the position (0, 6).

associated with this object ($d = 415$ pc) (Johnston, Sloanaker, & Bologna 1973). Barnes & Crutcher (1990) observed a torus around this source, perpendicular to the outflow (see also Lis et al. 1991). Like NGC 2024 FIR 5, a low-velocity shoulder was detected in the HCO^+ $J = 3$–2 line (Fig. 5).

3.10. *HH 25MMS*

This source ($d = 400$ pc) is within the L1630 cloud. Gibb & Heaton (1993) detected a CO outflow centered on this source. Bontemps, André, & Ward-Thompson (1995) identified this source as either a class 0 or a class I source. The HCO^+ $J = 4$–3 line at the central position has a clear blue asymmetry, but the HCO^+ $J = 3$–2 line is only slightly asymmetric (Figs. 1 and 2).

3.11. *IRAS 08076−3556*

This source ($d = 400$ pc) is located in the Gum Nebula and is the exciting star of HH 120. It has a steep spectral index in the infrared (Persi et al. 1990). Persi et al. (1994) noted that the 1.3 mm continuum flux was similar to those of other class 0 sources. Our calculated T_{bol}, 74 ± 15 K, puts it on the boundary of the class 0 category. Our observations show a symmetric line in HCO^+ $J = 4$–3 and a slight blue asymmetry in $J = 3$–2 (Figs. 5 and 6).

3.12. *VLA 1623*

This source ($d = 125$ pc), the prototype for the class 0 category, has a highly collimated CO outflow that extends over 15′ in length (André et al. 1990a; Dent, Matthews, & Walther 1995). AWB (1993) argued that the low temperature, high extinction, and massive envelope of VLA 1623 were evidence of an extremely young object. Our observations are ambiguous regarding collapse. The HCO^+ $J = 3$–2 and HCO^+ $J = 4$–3 lines both have a three-peaked spectrum with red asymmetry (Figs. 3 and 4). The $H^{13}CO^+$ $J = 3$–2 line peaks between the middle and the red peak of the HCO^+ $J = 3$–2 line (Fig. 3). These line profiles probably result from confusion with clumps in the outflow.

3.13. *IRAS 16293−2422*

Walker et al. (1986) reported the first observations of spectral line signatures of infall in this source ($d = 125$ pc).

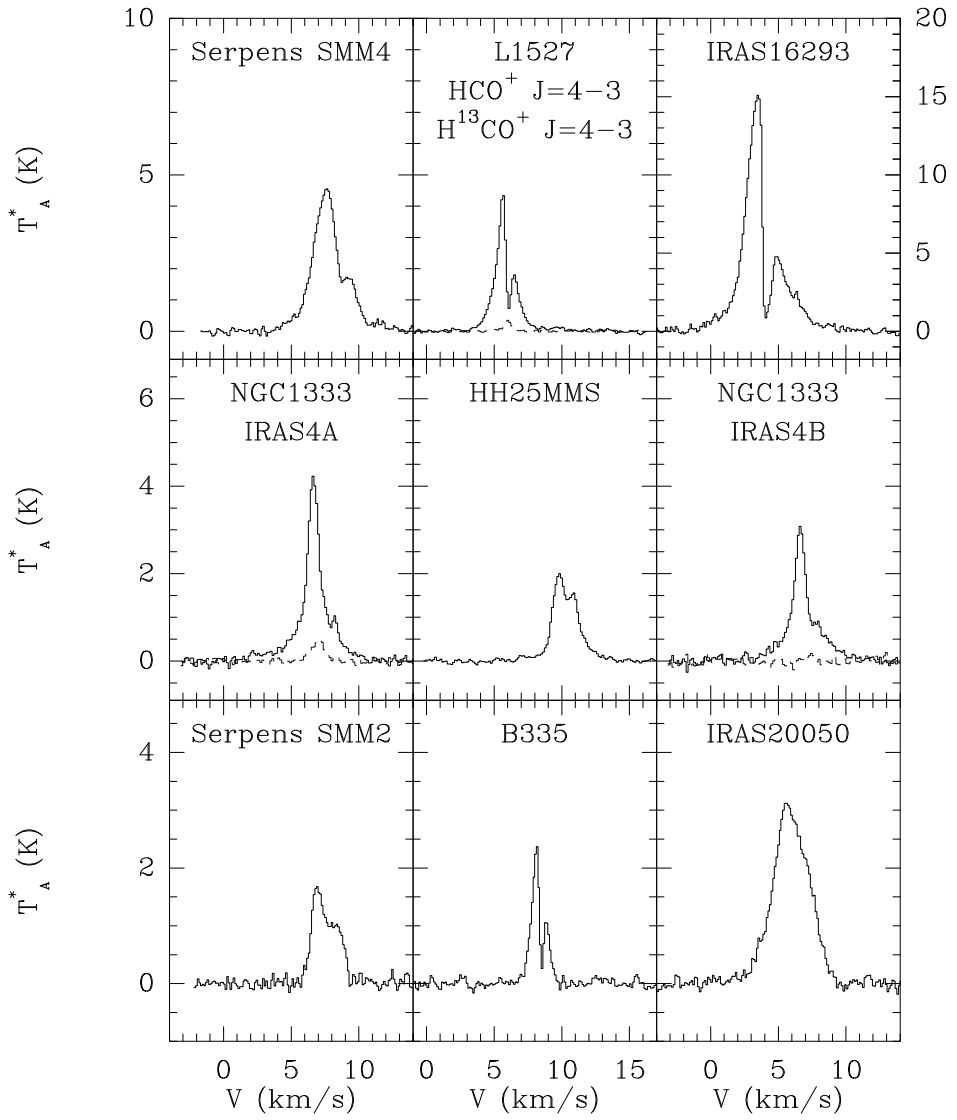

FIG. 2.—HCO^+ and, where available, $H^{13}CO^+$ $J = 4$–3 spectra toward the center of nine class 0 sources. These sources all show a blue asymmetry in the HCO^+ $J = 4$–3 line characteristic of collapse. The solid line is the HCO^+ spectrum, and the dashed line is the $H^{13}CO^+$ spectrum. The scale for the spectrum of IRAS 16293 is shown on the right-hand side of its panel.

Menten (1987) disputed this interpretation and claimed that the asymmetry was a rotational effect. However, Zhou (1995) has modeled this core as collapse with rotation. There is an elongated structure in the central region that was originally attributed to a disklike structure (Mundy, Wilking, & Myers 1986) but is now known to be a binary system with a separation of 5″ (Wootten 1989). The HCO^+ $J = 4$–3 and $J = 3$–2 lines are quite strong (15 K and 18 K, respectively) and have a clear infall signature (Figs. 1 and 2). Even the $H^{13}CO^+$ $J = 3$–2 line shows central self-absorption (Fig. 1), suggesting it is optically thick, as van Dishoeck et al. (1995) found for the $J = 4$–3 line. Our detection of the $HC^{18}O^+$ $J = 3$–2 line (Fig. 7) would agree with the interpretation of van Dishoeck et al. The $HC^{18}O^+$ $J = 3$–2 line profile may have two peaks, suggesting self-absorption.

3.14. *L483*

The CO outflow ($d = 200$ pc) was observed by Parker, Padman, & Scott (1991), who noted its similarity to that of B335, in that it has some blue emission in the red lobe, and vice versa. Fuller & Myers (1993) traced the dense gas in the cloud with the HC_3N $J = 4$–3 line. An H_2O maser has been detected by Wilking et al. (1994). Fuller et al. (1995) calculated a T_{bol} of 46 K, similar to the 48 ± 5 K we calculated. Myers et al. (1995) observed a double-peaked line profile with a stronger blue peak in the H_2CO $J = 3_{12}$–2_{11} and $J = 2_{12}$–1_{11} lines. The HCO^+ $J = 3$–2 line profile has a red-peaked spectral line profile with $H^{13}CO^+$ $J = 3$–2 peaking to the red side of the dip, while the HCO^+ $J = 4$–3 line displays a slight red asymmetry (Figs. 3 and 4). Unlike the case of L1448-C, the velocities of the red and blue peaks in HCO^+ agree with those in the H_2CO spectra of Myers et al. The fact that HCO^+ has a red asymmetry weakens the case for collapse.

3.15. *Serpens SMM1*

This source in Serpens ($d = 310$ pc) is also known as FIRS1 (Harvey, Wilking, & Joy 1984). Casali, Eiroa, & Duncan (1993) detected this source, discovered the next three sources in submillimeter and millimeter continuum photometry of the Serpens molecular cloud core, and noted

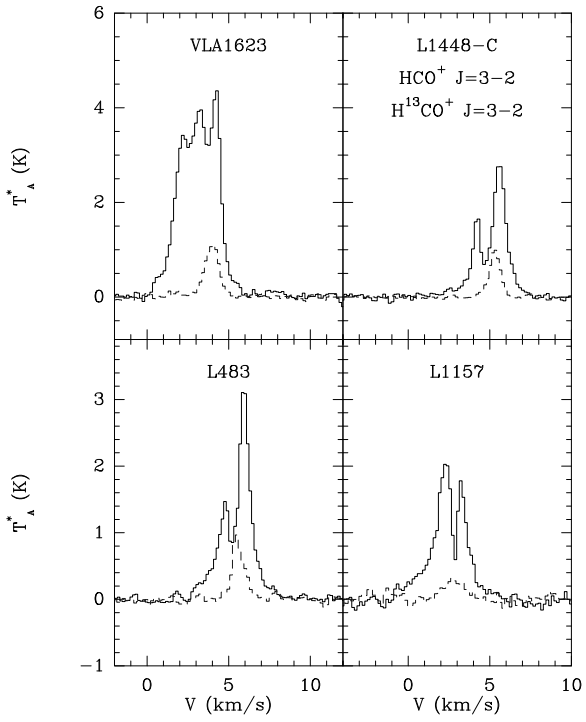

Figure 3

FIG. 3.—HCO^+ and $H^{13}CO^+$ $J = 3$–2 spectra toward the center of four class 0 sources. The first three sources, VLA 1623, L1448-C, and L483, all show a red asymmetry in the HCO^+ $J = 3$–2. L1157 has blue asymmetry in HCO^+ $J = 3$–2. The solid line is the HCO^+ spectrum, and the dashed line is the $H^{13}CO^+$ spectrum.

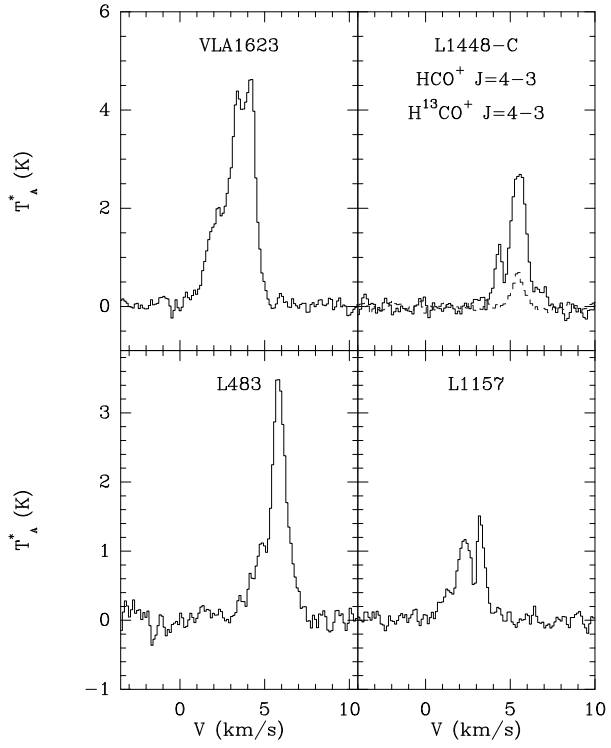

FIG. 4.—HCO^+ and, where available, $H^{13}CO^+$ $J = 4$–3 spectra toward the center of four class 0 sources. The first three sources, VLA 1623, L1448-C, and L483, also have a red asymmetry in the HCO^+ $J = 3$–2. L1157, which has blue asymmetry in HCO^+ $J = 3$–2, shows a red signature in $J = 4$–3. The solid line is the HCO^+ spectrum, and the dashed line is the $H^{13}CO^+$ spectrum.

the lack of near-IR counterparts, a trait that many other class 0 objects share. However, they also pointed out that this could be a more evolved object because a nearby jet shows reflected 2 μm emission from a possible hot source at the center. Hurt, Barsony, & Wootten (1996) observed a double-peaked and symmetric line profile with a dip at 9 km s^{-1} in the $J = 3_{03}$–2_{02} line of H_2CO. The HCO^+ $J = 4$–3 and $J = 3$–2 lines reveal quite strong self-absorption of a symmetric line, suggesting a large optical depth (Figs. 5 and 6), but there is no collapse signature, in agreement with Hurt et al. (1996).

3.16. *Serpens SMM4*

This source ($d = 310$ pc) and the following two sources were discovered in the submillimeter continuum maps of Casali et al. (1993). Hurt et al. (1996) saw a slight scallop at 8.75 km s^{-1} in the $J = 3_{03}$–2_{02} line of H_2CO. The HCO^+ $J = 4$–3 and $J = 3$–2 lines display a strong blue asymmetry (Figs. 1 and 2). The $H^{13}CO^+$ $J = 3$–2 line peaks in the self-absorption dip of the HCO^+ $J = 3$–2 line, which agrees in velocity with the dip in the 218 GHz H_2CO line.

3.17. *Serpens SMM2*

The 218 GHz H_2CO line shows two peaks (Hurt et al. 1996). A slight blue asymmetry can be seen in the HCO^+ $J = 3$–2 line at the central position ($d = 310$ pc). The blue asymmetry is also present in the HCO^+ $J = 4$–3 line, but it is not as prominent (Fig. 2). The $H^{13}CO^+$ $J = 3$–2 line has two velocity components at the same velocity as the two peaks of the HCO^+ $J = 3$–2 line (Fig. 1), suggesting that two cloud components exist in this region rather than collapse. The $HC^{18}O^+$ $J = 3$–2 line (Fig. 7) has one component, but higher signal-to-noise observations are needed.

3.18. *Serpens SMM3*

A blue outflow wing can be seen in the HCO^+ $J = 3$–2 line, but the central line core ($d = 310$ pc) displays no asymmetry in either the HCO^+ $J = 4$–3 or $J = 3$–2 line (Figs. 5 and 6).

3.19. *L723*

Davidson (1987) identified this far-infrared and submillimeter source ($d = 300$ pc). The outflow of this cloud has a quadrupolar structure (Goldsmith et al. 1984), which Avery, Hayashi, & White (1990) interpreted as the limb-brightened walls of a cavity. Anglada et al. (1991) found two radio continuum sources within L723, suggesting two outflows, but Cabrit & André (1991) reported a single source. The class 0 identification (Cabrit & André) is supported by our calculation of $T_{bol} = 39$ K. Our HCO^+ observations show a symmetric line (Figs. 5 and 6).

3.20. *B335*

B335 is a well-studied class 0 source ($d = 250$ pc). Zhou et al. (1990) mapped the 6 cm H_2CO line in this source and found a density gradient consistent with the Shu (1977) model of inside-out collapse. More direct evidence of collapse was found by Zhou et al. (1993) with the observation of an asymmetric spectral line signature in the CS $J = 2$–1 and $J = 3$–2 lines and the 140 and 225 GHz lines of H_2CO. Choi et al. (1995) have modeled the line profiles of Zhou et al. (1993) as inside-out collapse. Velusamy, Kuiper, & Langer (1996) have seen clumpy structure in the infalling envelope. Our central position is taken from the 2.7 mm

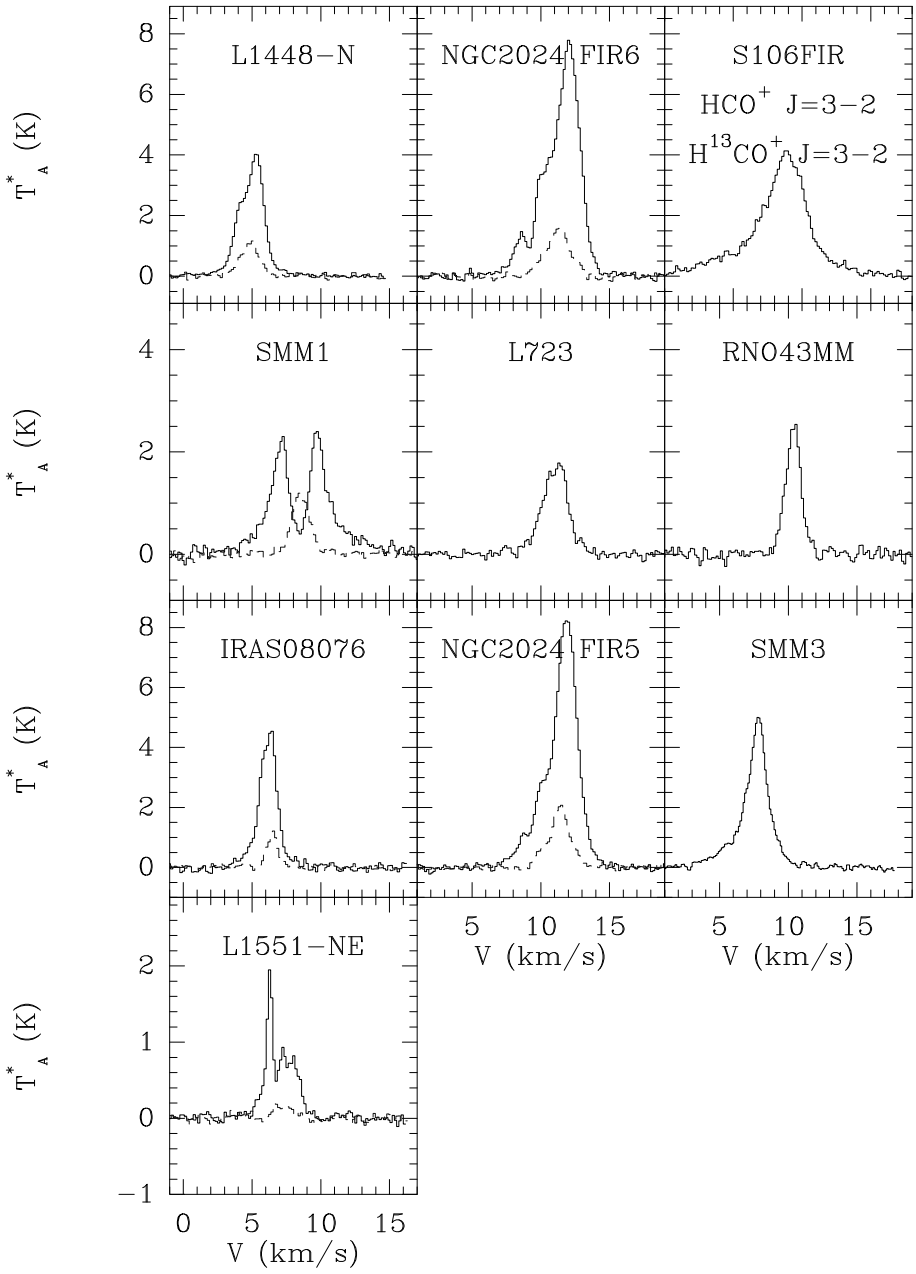

FIG. 5.—HCO^+ and, where available, $H^{13}CO^+$ $J = 3$–2 spectra toward the center of 10 class 0 sources. Most of these sources do not show any clear asymmetry in the HCO^+ $J = 3$–2 line. The solid line is the HCO^+ spectrum, and the dashed line is the $H^{13}CO^+$ spectrum.

continuum observations of Chandler & Sargent (1993). Our HCO^+ observations also show an infall signature (Figs. 1 and 2).

3.21. *IRAS 20050+2720*

This core ($d = 700$ pc) was included in the sample of cold IRAS sources of Wilking et al. (1989b). The value of 69 ± 7 for T_{bol} places it barely within the category of class 0 objects. However, it is considerably more luminous than the other sources. Recently, Bachiller, Fuente, & Tafalla (1995) discovered an outflow with three pairs of lobes, suggesting more than one central star. One outflow has an extremely high-velocity jet with molecular bullets like L1448-C. The CS $J = 3$–2 and $C^{34}S$ $J = 3$–2 line observations of Bachiller et al. (1995) show the optically thin $C^{34}S$ peaking at 6.1 km s^{-1}, quite close to the CS self-absorption dip at 6 km s^{-1}. Chen et al. (1997) have detected a cluster of 200 near-infrared sources. The HCO^+ $J = 3$–2 data show a broad double-peaked line toward the center. The $H^{13}CO^+$ $J = 3$–2 line peaks in the absorption dip of the HCO^+ $J = 3$–2 line but is rather broad (Fig. 1). The HCO^+ $J = 4$–3 line shows a slight blue asymmetry toward the central position (Fig. 2).

3.22. *S106FIR*

This source ($d = 600$ pc) lies in the bipolar nebula S106. S106 is bisected by a dark lane that possibly contains a disk (Bally, Snell, & Predmore 1983). However, more recent observations have shown that was what believed to be a disk is actually several clumps (Barsony et al. 1989; Richer et al. 1993). This source was first detected by Richer et al. in continuum maps at 450, 850, and 1100 μm at a position 15″

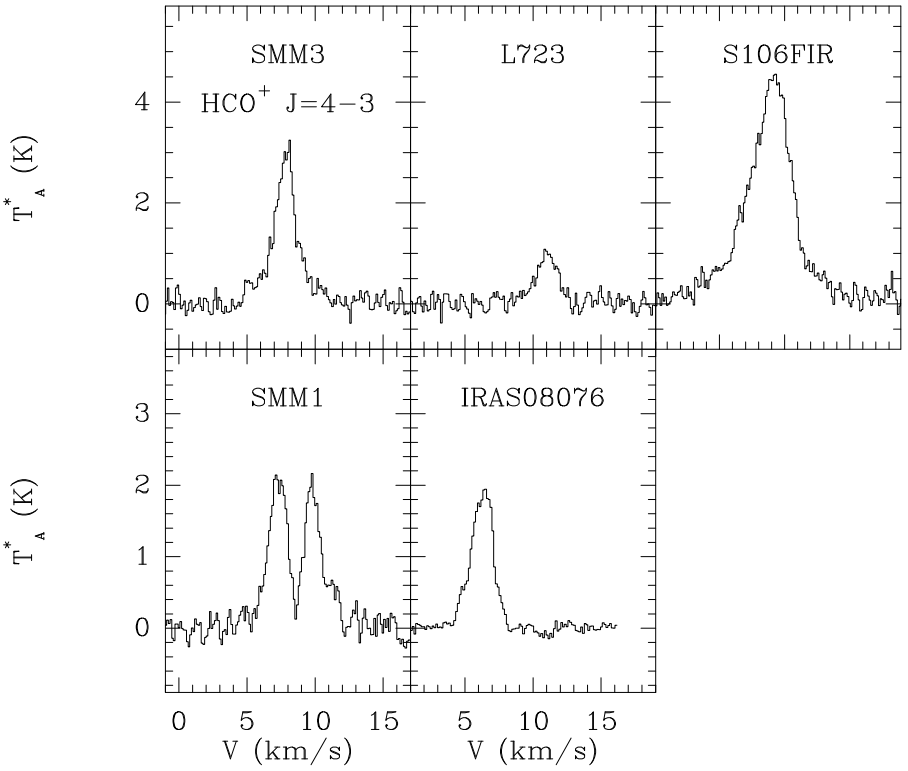

FIG. 6.—HCO^+ $J = 4$–3 spectra toward the center of five class 0 sources. These sources do not show any clear asymmetry in the HCO^+ $J = 4$–3 line.

west of S106IR. Its position coincides with an H_2O maser (Stutzki, Ungerechts, & Winnewisser 1982). No asymmetry was detected, but broad line wings, possibly from an outflow, were seen in the HCO^+ $J = 4$–3 and $J = 3$–2 lines (Figs. 5 and 6).

3.23. *L1157*

This source ($d = 440$ pc) has a well-collimated CO outflow in which the blue lobe of the outflow seems to be shock heating the ambient gas (Umemoto et al. 1992). Tafalla & Bachiller (1995) pointed out that the SED is quite similar to that of a class 0 object; we find $T_{bol} \lesssim 44$ K. Our HCO^+ $J = 3$–2 data shows the required blue asymmetry for collapse, but the HCO^+ $J = 4$–3 line shows the opposite asymmetry (Figs. 3 and 4). The blue outflow wing is quite clear at the center position in HCO^+ $J = 3$–2. The $H^{13}CO^+$ $J = 3$–2 line peaks in the self-absorption dip of the HCO^+ $J = 3$–2 line.

4. DISCUSSION

The line profiles in nine sources are consistent with predictions of line profiles from collapsing clouds. Caution is suggested by the fact that three sources show the opposite asymmetry and one shows different asymmetries in different lines. In this section, we will present some predictions for the expected shape of HCO^+ lines in collapsing clouds. We will then use these predicted line profiles to get quantitative measures of the line asymmetry that can be compared with the same measures for the observations. We will then discuss the effects of outflows on the spectra and present some detailed modeling of one source, L1527. Based on these considerations, we will construct a truth table (Table 6) to help decide which sources are good collapse candidates (§ 5).

4.1. *Evolutionary Modeling*

Zhou (1992) has modeled the behavior of CS lines as a function of time in a collapsing cloud. He found that the CS lines get broader, weaker, and more asymmetric as the collapse proceeds, as a result of the rising velocities and dropping densities inside the infall radius. Because HCO^+ has different optical depth and excitation properties, the detailed behavior of its line profiles may differ from those of CS. Consequently, we have modeled the evolution of the HCO^+ $J = 3$–2 and $J = 4$–3 line profiles, as well as the $H^{13}CO^+$ $J = 3$–2 and $J = 4$–3 lines, with time. We used the density and velocity fields of the inside-out collapse model (Shu 1977) and a temperature distribution derived from scaling that used for B335 (Zhou et al. 1990) to a luminosity of 6.5 $L_\odot$, the average luminosity of the sources with well-determined bolometric temperatures. The sound speed, a, was set at 0.21 km s^{-1}. Altering the sound speed would slow down or speed up the evolution of the line profile. Models were run for infall radii, r_{inf}, of 0.005, 0.01, 0.02, 0.03, 0.04, 0.05, 0.06, and 0.08 pc, corresponding to infall times of 2.3×10^4 yr for the earliest model and 3.8×10^5 yr for the last. The models had 30 shells, 15 inside the infall radius and 15 outside the infall radius. The outer radius, r_{out}, was 0.2 pc. Changing the outer radius affects the line profile very little. We used a constant abundance of $X(HCO^+) = 6 \times 10^{-9}$. The terrestrial abundance ratio of $X(HCO^+)/X(H^{13}CO^+) = 90$ was assumed. The H_2-HCO^+ collisional rate coefficients are taken from Monteiro (1985) for levels up to $J = 4$; the rate coefficients for $J = 5$ and 6 are scaled appropriately from those calculated by Green (1975) for N_2H^+.

These parameters were used as input into a code that simulates the Shu infall model and includes the temperature and abundance distribution. The resulting output, the

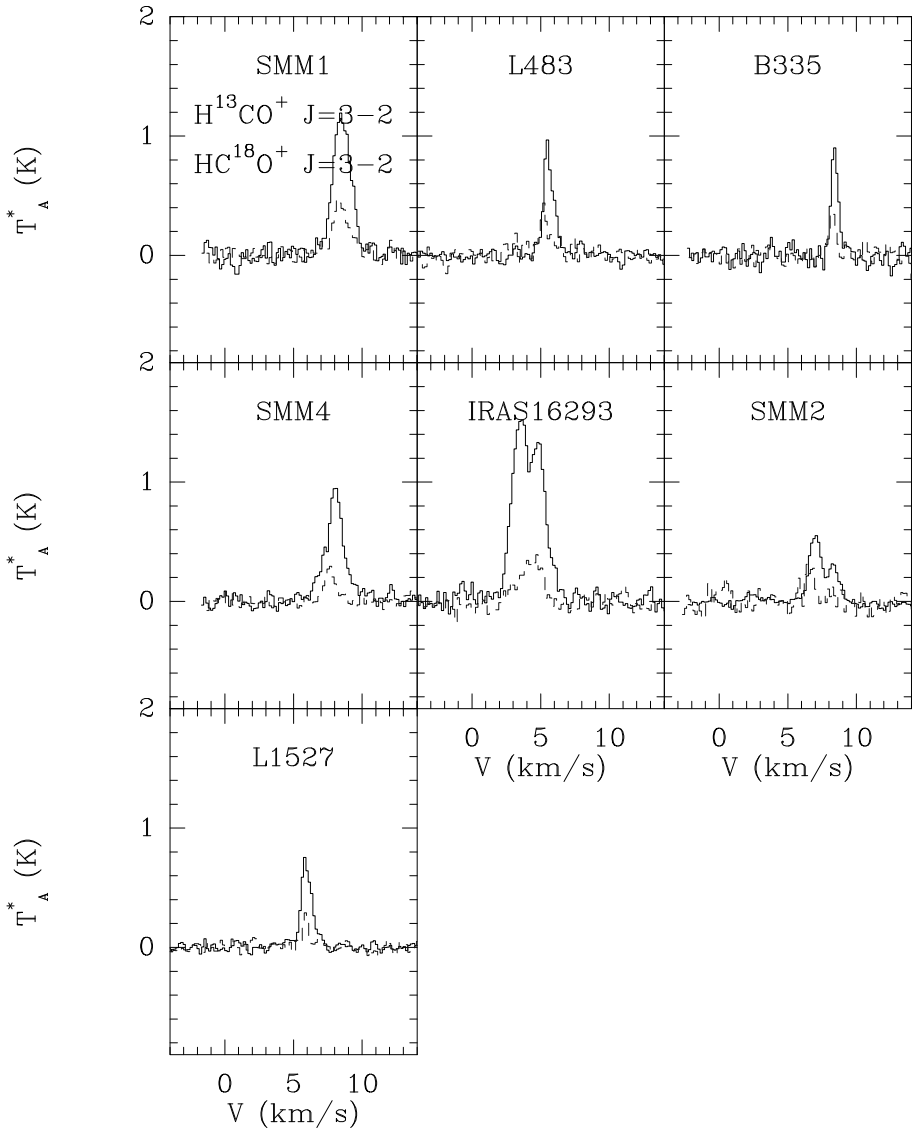

FIG. 7.—$H^{13}CO^+$ and $HC^{18}O^+$ $J = 3$–2 spectra toward the center of six class 0 sources. The solid line is the $H^{13}CO^+$ spectrum, and the dashed line is the $H^{18}CO^+$ spectrum. In all of these sources, the $HC^{18}O^+$ $J = 3$–2 has been scaled up by 2 except for L483, SMM2, and B335, where the $HC^{18}O^+$ $J = 3$–2 has been scaled up by a factor of 4.

density, velocity, kinetic temperature, turbulent width, and $X(HCO^+)$ at each shell, was then fed into the Monte Carlo code described by Choi et al. (1995). The output of this code, populations of each level of HCO^+ in each shell, then became the input to a virtual telescope program that simulated observations with the CSO, convolving the emission from each shell with the spatial and velocity resolution of the actual observations (Fig. 8). The distance to the model cloud was 140 pc, which is the distance to the Taurus Molecular Cloud and only slightly farther than sources in the Ophiuchus cloud core ($d = 125 \pm 25$ pc) (de Geus, de Zeeuw, & Lub 1989).

The line profiles that emerge from these calculations are qualitatively similar to those of CS calculated by Zhou (1992), but some important differences emerge because of the difference between CS and HCO^+. The asymmetry between blue and red peaks increases with age, and it is stronger than in the CS profiles. Unlike the CS models, the intensity of the HCO^+ $J = 3$–2 line grows with time until $t \sim 1.9 \times 10^5$ yr because the dropping opacity outweighs the effects of dropping density. The $J = 4$–3 line also grows initially, but it decreases after $t = 9.4 \times 10^4$ yr since it is more sensitive to density. The $H^{13}CO^+$ $J = 3$–2 and $J = 4$–3 lines decrease with age and become clearly weaker than the observations after a very short time and before the blue-red asymmetry matches the observations. To get stronger $H^{13}CO^+$ lines while maintaining an isotope ratio of 90, we increased the abundance to $X(HCO^+) = 6 \times 10^{-8}$ inside the infall radius, while retaining $X(HCO^+) = 6 \times 10^{-9}$ in the static envelope, based on some models of Rawlings et al. (1992), which have lower HCO^+ abundances in the outer envelope than in the interior. These models (Fig. 9) can reproduce the observed $H^{13}CO^+$ lines, but the HCO^+ lines are now very opaque. One consequence is that the intensities of both $J = 3$–2 and $J = 4$–3 lines increase with time, as the opacity drops, until even later times.

Models were also run for a range of distances from 70 pc to 700 pc to check the effect of distance on the observed line profiles, as observed with a beam of fixed angular extent.

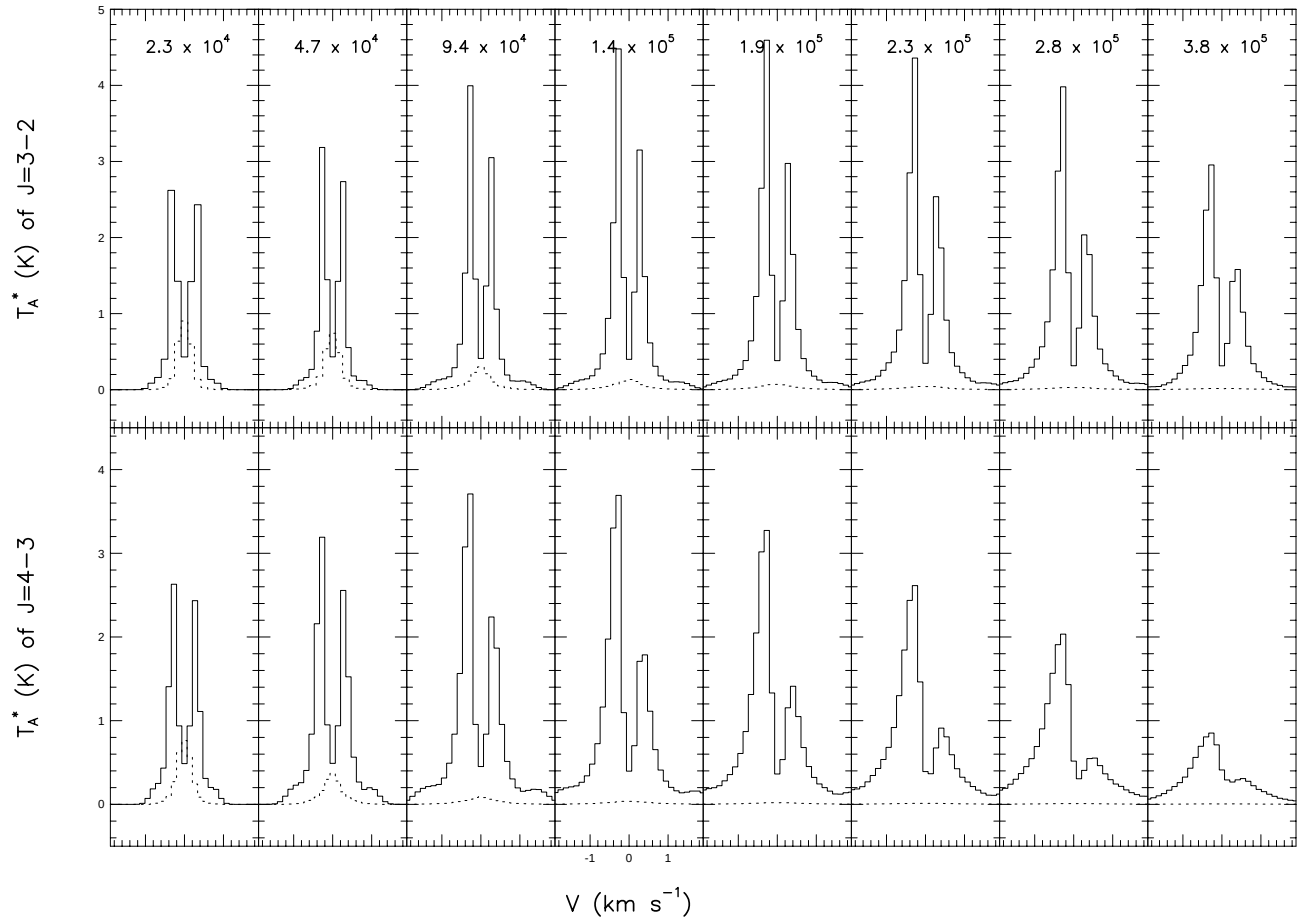

FIG. 8.—The top panel is a set of eight models following the temporal evolution of the HCO^+ (*solid line*) and $H^{13}CO^+$ (*dashed line*) $J = 3$–2 line profiles for a constant abundance $X(HCO^+) = 6 \times 10^{-9}$. The bottom panel shows the temporal evolution of the HCO^+ and $H^{13}CO^+$ $J = 4$–3 line profiles. The times since infall began are given in the upper panels and are the same in the lower panels.

The blue/red ratio decreases with distance from as high as 3.52 to as low as 1.59 for our constant abundance model. At 700 pc, the line profiles become noticeably asymmetric only at the oldest times. The line width and line strength also decrease with distance. All these effects will make collapse harder to detect in more distant clouds of low luminosity. However, the more distant sources are often more luminous, and the temperature distribution we used (appropriate for the average luminosity of our sample) will underestimate the line strength. Because of the dependence on distance, temperature, and abundance, we consider the models presented here only as rough sketches of the evolution of a collapsing cloud.

4.2. *Quantitative Collapse Indicators*

We can use the models of line profiles to predict the behavior of various quantities with time. For example, the asymmetry of the line profile can be characterized in various ways. One is the ratio of the blue peak intensity and the red peak intensity. The blue/red ratio is plotted versus time in Figure 10 for both lines and both models of the abundance. The blue/red ratio generally increases with time for both models of abundance and both lines, but the values are clearly larger for the model with constant abundance. Thus absolute values of the blue/red ratio cannot be used to assign an age without further information on the abundance.

For lines that are not clearly double-peaked, the blue/red ratio will be undefined, but we can still characterize the asymmetry of the line by a measure like the skewness. The skewness is a nondimensional quantity defined as the ratio of the third moment of a distribution and the 3/2 power of the second moment, both normalized by the first moment. We calculated the skewness as follows:

$$\text{skewness} = \frac{\sum [T_A^*(v - v_{\rm LSR})^3 \delta v]}{\sum (T_A^* \delta v)} \Bigg/ \left\{ \frac{\sum [T_A^*(v - v_{\rm LSR})^2 \delta v]}{\sum (T_A^* \delta v)} \right\}^{3/2}, \quad (1)$$

where $v_{\rm LSR}$ is the central velocity of the source and δv is the channel width. Line profiles with a negative skewness have a blue asymmetry, and sources with a positive skewness have a red asymmetry. The skewness of the model line profiles is also plotted in Figure 10. The skewness rapidly becomes more negative with time but eventually reaches a maximum negative value.

We have measured the blue/red ratio and skewness of the observed HCO^+ $J = 3$–2 and $J = 4$–3 lines to see how

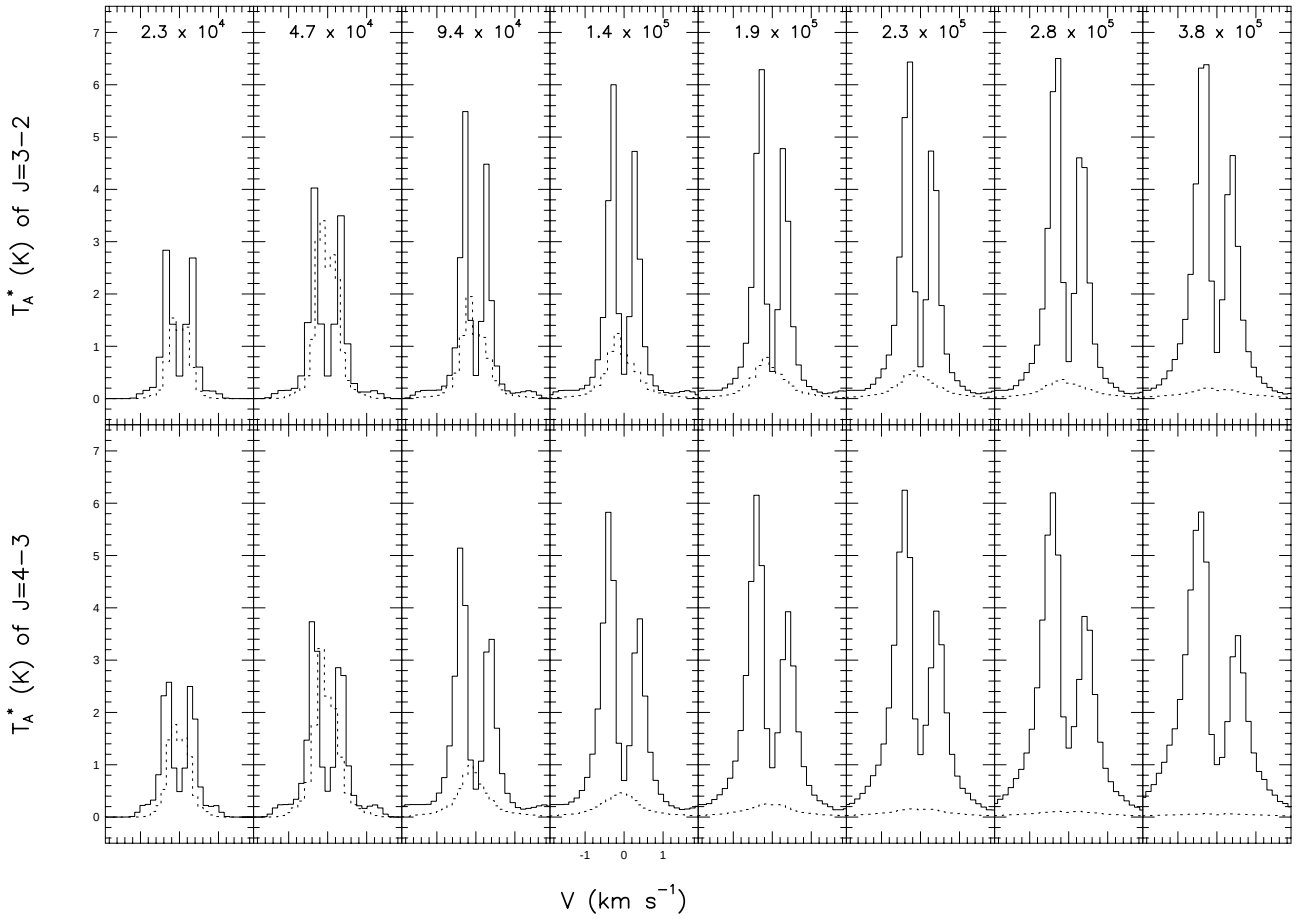

FIG. 9.—The same as Fig. 8, but with $X(HCO^+) = 6 \times 10^{-8}$ inside the infall radius and $X(HCO^+) = 6 \times 10^{-9}$ in the static envelope outside the infall radius.

these quantities compare to the model values (see Table 5). Lines with a single peak, even if skewed, or three peaks were assigned a blue/red ratio of one. Skewness was measured in the interval of $v_{LSR} \pm 1.25$ km s^{-1}. The v_{LSR} of the source was calculated from the velocity centroid of the optically thin $H^{13}CO^+$ line. This velocity interval was chosen because it covered the central line core for all the sources while excluding as much of the outflow wings as possible. (Changing the velocity interval over which the skewness is measured to 0.95 km s^{-1} or 2 km s^{-1} causes, at most, a 25% change in the skewness. The sign is unchanged.) As can be seen from Table 5 and Figure 11, all the double-peaked blue asymmetric sources, save the HCO^+ $J = 4$–3 line in Serpens SMM2, have a negative skewness. One of the two red asymmetric double-peaked sources, L483, has a positive skewness in $J = 4$–3 and zero skewness in $J = 3$–2; the other, L1448-C, has a negative skewness. It is possible to have a line with red asymmetry and negative or zero skewness if the line profile displays strong blue wings.

In Figure 11, we plot the skewness versus the blue/red ratio. The observed sources are represented by pentagons and the models as triangles ($J = 3$–2 line) or boxes ($J = 4$–3 line) connected by solid or dashed lines, according to the same scheme as in Figure 10. The good collapse candidates (§ 4.3) are shown as filled pentagons. The sources with a blue/red ratio greater than unity have negative skewness, as expected. The $J = 4$–3 lines lie nicely in the region of the models, but many of the $J = 3$–2 lines have larger blue/red ratios than are achieved in the models. In this plot, the difference between the two models is small, except that the model with constant abundance extends to much higher blue/red ratios and covers the region with quite a few sources in the $J = 4$–3 line. In Figure 12, we show the blue/red ratio versus the peak line temperature. This plot reveals another difference between the data and the models: a number of sources have considerably stronger lines than are seen in either model. The arrow at the right indicates IRAS 16293, which lies off the plot. Some of these sources have higher luminosity and consequently higher temperatures than we have modeled; higher temperatures would produce stronger lines. For the $J = 4$–3 line, we can imagine that intermediate values of abundance may match the sources with blue/red ratios above two and line strengths greater than 2 K, but the high blue/red ratios in the $J = 3$–2 line may be harder to explain. This figure also reveals that high peak temperatures and high blue/red ratios are hard to achieve with the models we have run, probably because the assumed luminosity is lower than that of many of the sources.

4.3. *Outflow versus Infall*

Many of the spectra in Figures 1–6 show substantial high-velocity wings, which are not produced in the infall models of the last section. Models with faster infall or

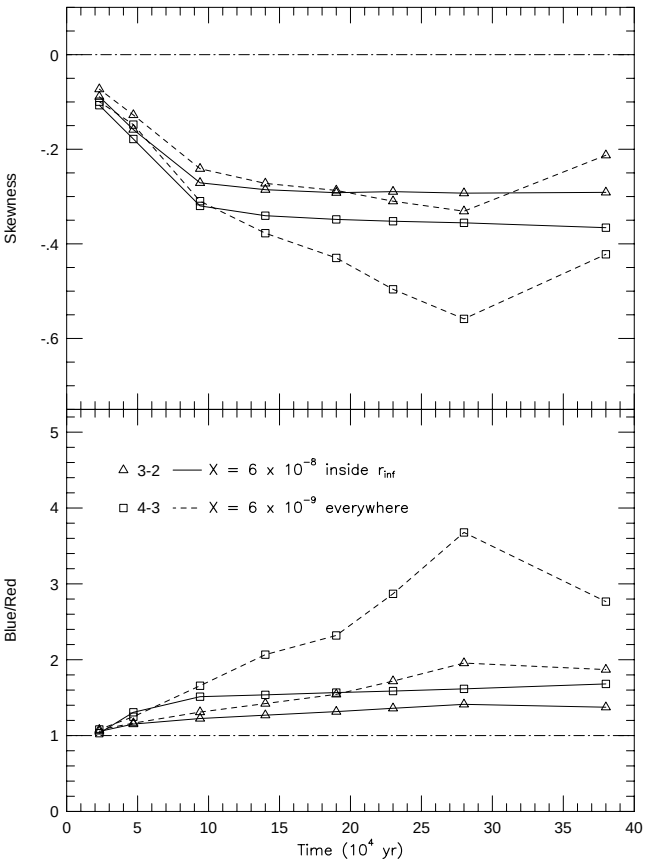

FIG. 10.—The top panel is the skewness of our evolutionary line profiles vs. time. The bottom panel is the blue/red ratio of our evolutionary line profiles vs. time. A Gaussian line would have a skewness of 0 and a blue/red ratio of 1 (*dash-dotted line*).

TABLE 5

VARIOUS COLLAPSE INDICATORS FOR HCO^+

Source	Line	Skewness	Blue/Red
L1448-N	$J = 3$–2	0.18 ± 0.29	1.00
L1448-C	$J = 4$–3	-0.50 ± 0.42	0.47
	$J = 3$–2	-0.26 ± 0.42	0.60
NGC 1333 IRAS 4A	$J = 4$–3	-0.33 ± 0.24	4.09
	$J = 3$–2	-0.65 ± 0.27	4.17
NGC 1333 IRAS 4B	$J = 4$–3	-0.56 ± 0.22	3.37
	$J = 3$–2	-0.45 ± 0.25	4.22
L1551-NE	$J = 3$–2	-0.34 ± 0.21	1.00
L1527	$J = 4$–3	-0.54 ± 0.19	2.39
	$J = 3$–2	-0.40 ± 0.22	2.02
RNO 43MM	$J = 3$–2	-0.58 ± 0.53	1.00
NGC 2024 FIR 5	$J = 3$–2	0.42 ± 0.20	1.00
NGC 2024 FIR 6	$J = 3$–2	0.66 ± 0.20	1.00
HH 25MMS	$J = 4$–3	-0.18 ± 0.22	1.30
	$J = 3$–2	-0.44 ± 0.20	1.00
IRAS 08076	$J = 4$–3	-0.46 ± 0.25	1.00
	$J = 3$–2	-0.94 ± 0.38	1.00
VLA 1623	$J = 4$–3	-0.97 ± 0.23	1.00
	$J = 3$–2	-0.86 ± 0.27	1.00
IRAS 16293	$J = 4$–3	-0.66 ± 0.11	3.17
	$J = 3$–2	-0.38 ± 0.14	2.64
L483	$J = 4$–3	0.15 ± 0.30	0.32
	$J = 3$–2	-0.01 ± 0.28	0.47
Serpens SMM1	$J = 4$–3	-0.22 ± 0.10	0.99
	$J = 3$–2	0.09 ± 0.12	0.96
Serpens SMM4	$J = 4$–3	-0.41 ± 0.15	2.64
	$J = 3$–2	-0.83 ± 0.19	3.05
Serpens SMM3	$J = 4$–3	-0.20 ± 0.24	1.00
	$J = 3$–2	-0.48 ± 0.16	1.00
Serpens SMM2	$J = 4$–3	0.08 ± 0.16	1.63
	$J = 3$–2	-0.27 ± 0.12	1.16
L723	$J = 4$–3	-0.01 ± 0.44	1.00
	$J = 3$–2	0.05 ± 0.30	1.00
B335	$J = 4$–3	-0.15 ± 0.46	2.25
	$J = 3$–2	-0.46 ± 0.53	2.08
IRAS 20050	$J = 4$–3	-0.15 ± 0.13	1.00
	$J = 3$–2	-0.13 ± 0.10	1.41
S106FIR	$J = 4$–3	-0.11 ± 0.14	1.00
	$J = 3$–2	-0.15 ± 0.24	1.00
L1157	$J = 4$–3	-0.37 ± 0.30	0.77
	$J = 3$–2	-0.25 ± 0.23	1.14

enhanced abundances of HCO^+ in the innermost parts of the infall might produce stronger line wings, but these would be concentrated toward the center of the infall. Maps of the distribution in space of the emission in different velocity ranges can distinguish between infall and bipolar outflow. The top two panels of Figure 13 are integrated intensity maps of one of our infall models. The simulated map, like the actual observations, was made with 15″ spacing. The integrated intensity of the two peaks is centered on the infrared source, and the red peak is more compact than the blue peak (Fig. 13). The emission in the line wings should be very compact. (The dashed contours are the integrated intensity of the redshifted peak and the red line wing.) Figure 13 also shows maps of the intensity integrated over different velocity intervals in L1527. The integrated blue and red line wing intensities are peaked on either side of the source, indicating that the line wings are due to outflow lobes and are clearly not related to collapse. The map of the velocity interval corresponding to the blue peak is fairly circular and peaks near the center position, but the red peak is somewhat displaced, indicating some contamination by the outflow. Several other sources (notably, NGC 1333 IRAS 4A, Serpens SMM4, L483, and L1448-C) have bipolar outflow emission in HCO^+, based on the maps of the line wings (Figs. 13, 14, and 15).

If bipolar outflows dominate the line wings, they might also dominate the peaks. In this case, a high blue/red ratio would not reflect collapse but, rather, the relative strength of the two bipolar lobes in the beam centered on the source. In that case, we might expect an equal number of sources to have stronger red peaks. Considering only the sources with two clearly distinct peaks, there are seven with stronger blue peaks and two with stronger red peaks; for a sample of nine objects with intrinsically equal probability for either peak to be stronger, the probability is only 0.07 that seven will have stronger blue peaks. Thus it is unlikely, but not impossible, that the peaks are all caused by outflows.

Despite the statistical evidence that not all the double-peaked spectra are caused by outflows, the chance of contamination by outflows is serious enough that we do not consider the HCO^+ data alone to be sufficient evidence for collapse. Instead, we take a blue asymmetry in both HCO^+ $J = 4$–3 and $J = 3$–2 as an indication of possible collapse worthy of further investigation. Of the nine sources with blue asymmetry, three (B335, IRAS 16293, and L1527) have been previously suggested as collapse candidates, based on other lines. Of the other six, Serpens SMM2 can probably be eliminated from consideration because the $H^{13}CO^+$ $J = 3$–2 line has two velocity components, which have nearly the same velocities as the two peaks of the HCO^+ $J = 3$–2 line. For the others, we can compare the integrated intensity maps of the peaks to those produced by an infall

TABLE 6

TRUTH TABLE

Source	Asymmetry 3–2	Asymmetry 4–3	$H^{13}CO^+$ Peaks in Dip	Line Peak Maps
L1448-N	r	...	y	...
L1448-C	r	r	close	n
NGC 1333 IRAS 4A	b	b	close	n
NGC 1333 IRAS 4B	b	b	y	n
L1551-NE	b	...	n	...
L1527	b	b	y	y
RNO 43MM	n	...	...	...
NGC 2024 FIR 5	n	...	n	...
NGC 2024 FIR 6	n	...	n	...
HH 25MMS	b	b	y	?
IRAS 08076	n	n	n	...
VLA 1623	r	r	y	?
IRAS 16293	b	b	y	y
L483	r	r	y	n
Serpens SMM1	n	n	y	...
Serpens SMM4	b	b	close	y
Serpens SMM2	b	b	n	?
Serpens SMM3	n	n	...	...
L723	n	n	...	...
B335	b	b	y	...
IRAS 20050	b	b	y	?
S106FIR	n	n	...	...
L1157	b	r	y	n

NOTE.—"r" = red asymmetry; "b" = blue asymmetry; "y" = the source satisfies the criterion; "n" = the source does not satisfy the criterion; "close" = the $H^{13}CO^+$ peaks between a peak and the dip of the HCO^+ line; "?" = the peaks overlap, but one is spread over a larger area than the other; "..." = no observations.

model. In NGC 1333 IRAS 4A and 4B, the blue peak is centered on IRAS 4A, but the red peak increases in intensity to the north. In Serpens SMM4, as in L1527, the two peaks are separated by about 10″ (Fig. 14), in the same direction that the peaks are displaced in the maps of the line wings, suggesting contamination from outflow emission. In HH 25MMS and IRAS 20050, the maximum of one peak stretches over a larger area than the other peak (Fig. 15). Since rotation will also cause a shift of peaks, these sources cannot be ruled out as collapse candidates, but more evidence would be needed.

It is noteworthy that both L483 and L1448-C, which have blue/red ratios less than one, have strong bipolarity in the integrated line wing emission (Fig. 15). In L1448-C, the blue peak is displaced from the center by about 15″, supporting our earlier suggestion that it is a feature in the outflow. In L483, the red peak and the blue peak are displaced about 20″ in an east-west direction, as are the peaks in the maps of the line wing emission. Also, in L483, the peaks are separated in the direction of the outflow.

Table 6 is a truth table, which includes information on whether the lines have the correct asymmetry for collapse and whether the $H^{13}CO^+$ line peaks in the self-absorption dip. Table 6 also includes information on whether the integrated intensity maps of the line peaks are compatible with collapse, with a "n" indicating that the maps of the line peaks are displaced in a way that suggest they are dominated by outflow.

4.4. *Detailed Modeling of L1527*

Given the uncertainties described above, we did not make detailed models of all the sources with blue asymmetries. Instead, we focused on L1527, a source with relatively good evidence for collapse (Zhou et al. 1994; Myers et al. 1995; Zhou, Evans, & Wang 1996), to see if the HCO^+ was consistent with previous models. Using the procedure described in § 4.1, we have modeled the spectra toward L1527. All models had an outer radius of 0.2 pc, a temperature distribution appropriate for the source luminosity (see § 4.1), and constant abundance. By comparing the model profiles to the observed $H^{13}CO^+$ $J = 4$–3 and $J = 3$–2 line profiles, we constrained the abundance for a range of infall radii. After scaling down the abundance in the $H^{13}CO^+$ models by a factor of 5, the predicted profiles for the $HC^{18}O^+$ $J = 4$–3 line are consistent with our upper limit of 0.07 K. Scaling the abundances that fit the $H^{13}CO^+$ profiles up by factors of 50 or 90 to model HCO^+, we found the model that best matches the observed line profiles, focusing on the inner part of the profiles to avoid the outflow (Fig. 16). This model has a constant abundance of $X(HCO^+) = 2.5 \times 10^{-8}$, 50 times the abundance of $H^{13}CO^+$. Models using 90 for the isotope ratio typically produced worse fits. The absorption dip is deeper in the model than in the observations, suggesting that a lower abundance in the static envelope would fit better. We did not pursue this point, to avoid introducing too many parameters. The best-fit model has an infall radius of 0.026 pc, in agreement with modeling of single-dish H_2CO spectra and interferometer data on ^{13}CO by Zhou et al. (1996), but larger than that found by Myers et al. (1995), $r_{inf} = 0.015$ pc, using different H_2CO data. The wings of the observed lines are clearly not produced by an infall model, and we attribute those to outflow as discussed earlier. Also, we have noted earlier that the integrated intensity maps of the line peaks show a $\sim 10''$ displacement between the two peaks in an east-west direction, as do the peaks in the maps of the line wing emission. Although the peak regions of the L1527 spectrum were used to determine the best-fitting model, there is still much excess emission in the peak regions. This emission is probably contamination from the outflow and contributes to the dis-

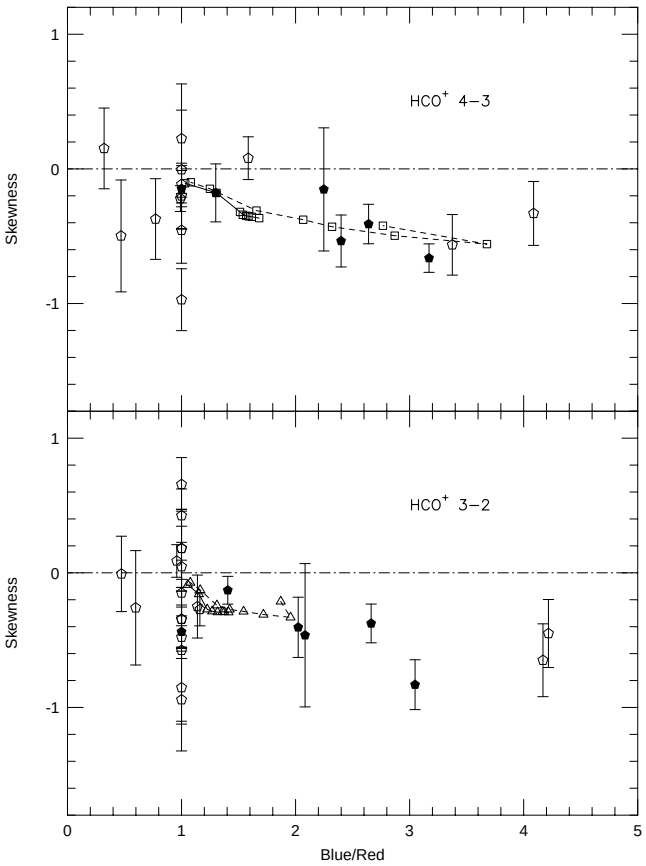

FIG. 11.—The top panel is the skewness of our observed line profiles vs. the blue/red ratio for the HCO^+ $J = 3$–2 line. The bottom panel is the skewness of our observed line profiles vs. the blue/red ratio for the HCO^+ $J = 4$–3 line. The triangular and the square points are the $J = 3$–2 and 4–3 lines from the models. The spectra from Fig. 8 are connected by a dashed line; those from Fig. 9, by a solid line. The open and filled pentagonal points are the class 0 sources and the good collapse candidates (see § 5), respectively. A blue/red value of 1 was was assigned to single- or triple-peaked lines.

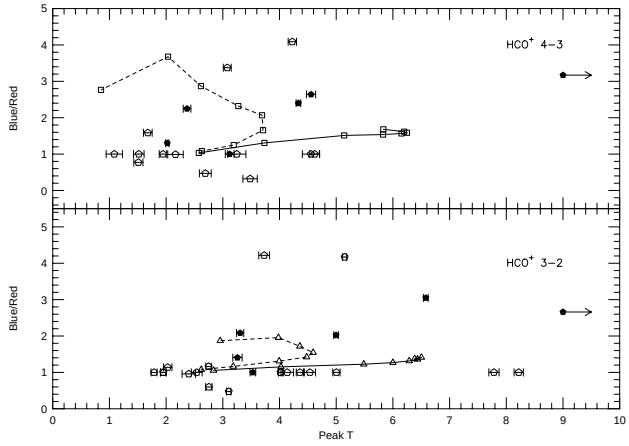

FIG. 12.—The top panel is the blue/red ratio of our observed line profiles vs. the peak temperature for the HCO^+ $J = 3$–2 line. The bottom panel is the blue/red ratio of our observed line profiles vs. the peak temperature for the HCO^+ $J = 4$–3 line. The triangular and the square points are the $J = 3$–2 and 4–3 lines from the models. The spectra from Fig. 8 are connected by a dashed line; those from Fig. 9, by a solid line. The open and filled pentagonal points are the class 0 sources and the good collapse candidates (see § 5), respectively. A blue/red value of 1 was was assigned to single- or triple-peaked lines.

placement of the two peaks seen in Figure 13. Note that the large blue/red ratio in the observations is not well matched by the models, as was also noted by Myers et al. (1995) in their modeling of the H_2CO $J = 2_{12}$–1_{11} line.

5. CONCLUSIONS

We have surveyed 23 class 0 sources in HCO^+ $J = 3$–2 and $J = 4$–3. Nine sources (39% of the sample) have a blue asymmetry, making them candidates for protostellar collapse. Three sources have a red asymmetry, and one source has different asymmetries in the two lines. The evolutionary progress of a collapsing core was modeled to provide predictions of what line profiles and statistical quantities that characterize them would look like. In general, the model line profiles are similar to the observed line profiles, but they have difficulty reproducing the large blue/red ratios seen in some sources.

HCO^+ shows the collapse signature quite well in sources previously identified as collapse candidates. According to chemical models, it may be relatively abundant in collapsing envelopes where other molecules may deplete (Rawlings et al. 1992). However, this molecule has some definite disadvantages. First, it emits strongly in outflowing gas, confusing collapse signatures. Second, it is a difficult molecule to model because its lines can be quite optically thick. We conclude that it is a good molecule for surveys of possible collapse candidates because its lines are strong, but confirmation with other molecular lines is needed before collapse can be definitely claimed.

Referring to Table 6, we find that B335, IRAS 16293, L1527 (all previously suggested), as well as HH 25MMS, Serpens SMM4, and IRAS 20050, are good candidates on all the criteria. NGC 1333 IRAS 4A and 4B meet the criteria other than the outflow maps. Serpens SMM2 fails the criterion that $H^{13}CO^+$ peaks in the dip.

We reiterate that these six sources are only collapse *candidates.* Before we can definitely say that protostellar collapse is happening in these sources, further work needs to be done. To strengthen the case for collapse, multitransition observations are needed in other optically thick molecules like CS and H_2CO. Also, two-dimensional modeling should be done to distinguish between the effects of collapse and rotation.

We would like to thank Yangsheng Wang, Daniel Jaffe, Wenbin Li, and Byron Mattingly for their help with observations. This work was supported by NSF grant AST-9317567.

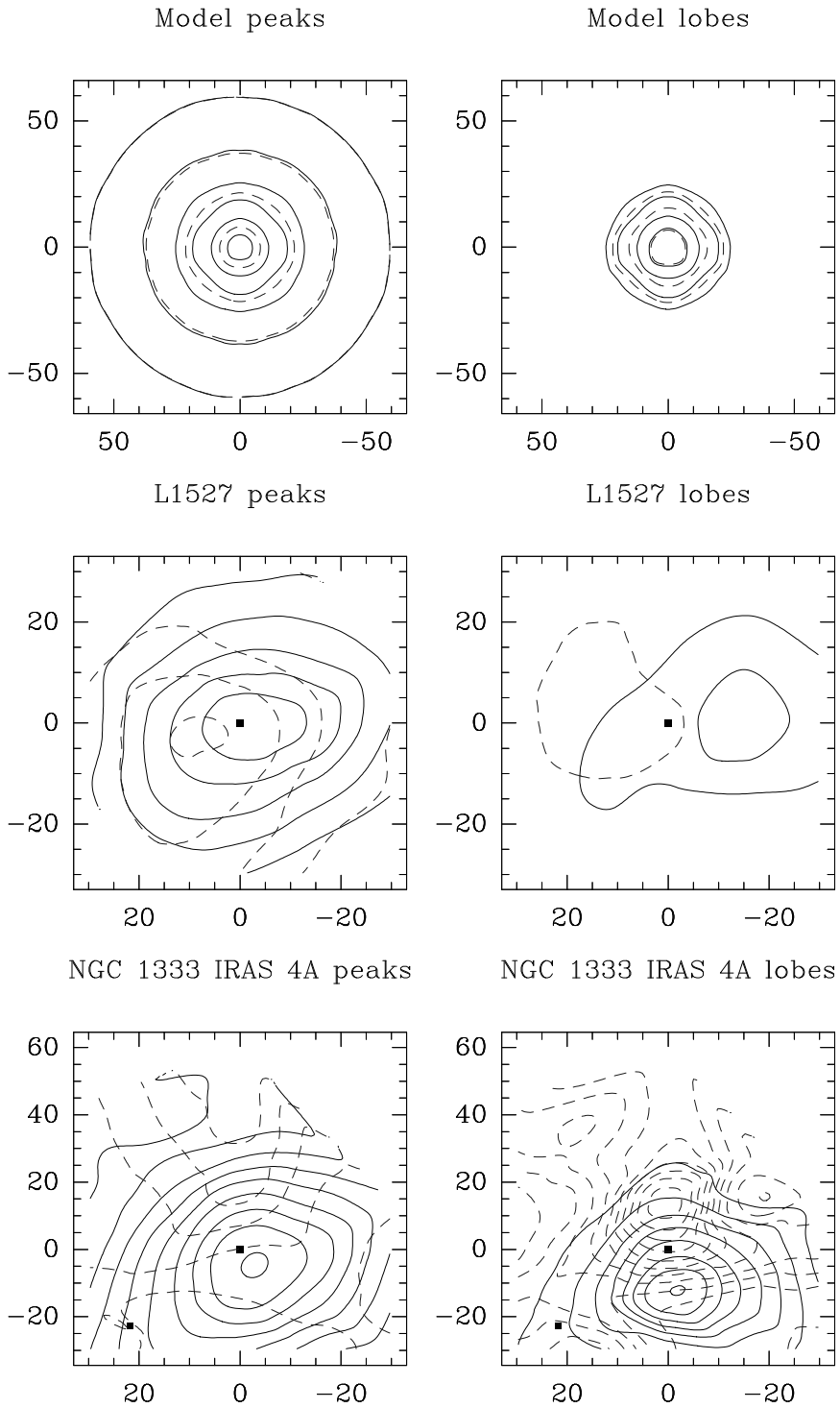

FIG. 13.—The top two plots are integrated intensity maps of the red and blue peaks and the blue and red lobes of the HCO^+ $J = 3$–2 line in a simulation of a collapsing cloud. The velocity intervals are -0.43 to -0.27 km s^{-1} and 0.27–0.43 km s^{-1} for the peaks and -3.09 to -0.43 km s^{-1} and 0.43–3.09 km s^{-1} for the lobes. The contour level spacing is 0.1 then 0.2 K km s^{-1} thereafter. In all plots, the solid contours are the blueshifted peak and the blue line wing and the dashed contours are the redshifted peak and the red line wing, respectively. The middle two plots are integrated intensity maps of the red and blue peaks and the blue and red lobes of the HCO^+ $J = 3$–2 line in L1527. The velocity intervals are 5–5.7 km s^{-1} and 6.1–7 km s^{-1} for the peaks and 2–5 km s^{-1} and 7–10 km s^{-1} for the lobes. The contour level spacing is 1 K km s^{-1} for the peaks and 0.5 K km s^{-1} for the lobes. The black square is the location of the IRAS source. The bottom two plots are integrated intensity maps of the red and blue peaks and the blue and red lobes of the HCO^+ $J = 3$–2 line in NGC 1333 IRAS 4A. The velocity intervals are 4.3–5.09 km s^{-1} and 5.7–6.33 km s^{-1} for the peaks and 2.6–4.3 km s^{-1} and 6.33–8.97 km s^{-1} for the lobes. The contour level spacing is 0.5 K km s^{-1} for the blue peak and blue lobe, 0.25 then 0.5 K km s^{-1} thereafter for the red peak, and 0.1 K km s^{-1} for the red lobe. The two black squares are the location of the submillimeter sources detected by Sandell et al. (1991). The source at (0, 0) is NGC 1333 IRAS 4A, and the source at (22, -23) is NGC 1333 IRAS 4B.

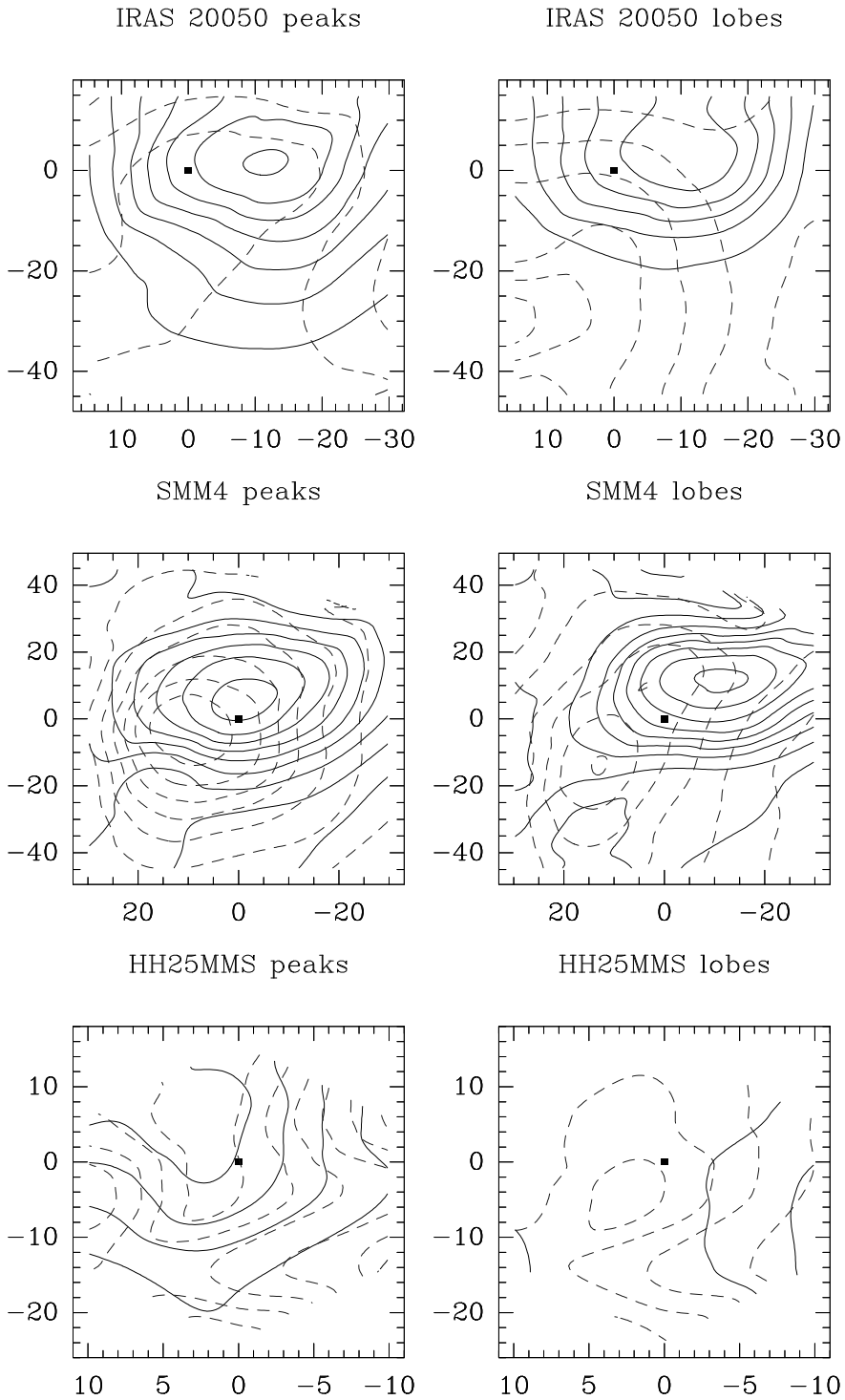

FIG. 14.—The top two plots are integrated intensity maps of the red and blue peaks and the blue and red lobes of the HCO^+ $J = 3$–2 line in IRAS 20050+2720. The velocity intervals are 4.62–5.91 km s^{-1} and 6.65–7.95 km s^{-1} for the peaks and -0.85 to 4.62 km s^{-1} and 7.95–10.74 km s^{-1} for the lobes. The contour level spacing is: 0.5 K km s^{-1} for the peaks, 1 then 0.5 K km s^{-1} thereafter for the blue lobe, and 0.4 K km s^{-1} for the red lobe. The black square is the location of the IRAS source. In all plots, the solid contours are the blueshifted peak and the blue line wing and the dashed contours are the redshifted peak and the red line wing, respectively. The middle two plots are integrated intensity maps of the red and blue peaks and the blue and red lobes of the HCO^+ $J = 3$–2 line in SMM4. The velocity intervals are 6.3–8.02 km s^{-1} and 9.09–10.03 km s^{-1} for the peaks and 2.42–6.3 km s^{-1} and 10.03–13.13 km s^{-1} for the lobes. The contour level spacing is 1 K km s^{-1} for the blue peak, 0.25 K km s^{-1} for the red peak, 0.5 K km s^{-1} for the blue lobe, and 0.3 K km s^{-1} for the red lobe. The black square is the location of the submillimeter continuum source (Casali et al. 1993). The bottom two plots are integrated intensity maps of the red and blue peaks and the blue and red lobes of the HCO^+ $J = 4 - 3$ line in HH 25MMS. The velocity intervals are 9.3–10.11 km s^{-1} and 10.51–11.3 km s^{-1} for the peaks and 7.17–9.3 km s^{-1} and 11.3–13.03 km s^{-1} for the lobes. The contour level spacing is 0.25 K km s^{-1} for the blue peak, 0.1 K km s^{-1} for the red peak, 0.18 K km s^{-1} for the blue lobe, and 0.15 K km s^{-1} for the red lobe. The black square is the location of the 1.3 mm radio continuum source (Bontemps et al. 1995).

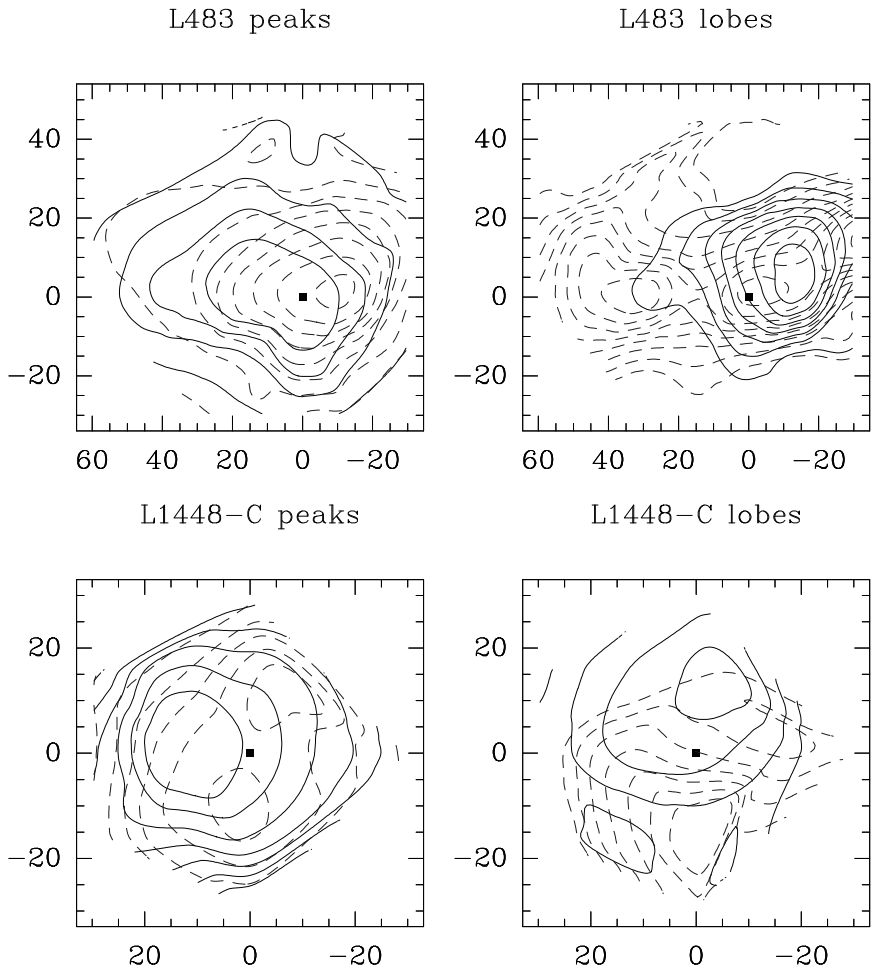

FIG. 15.—The top two plots are integrated intensity maps of the red and blue peaks and the blue and red lobes of the HCO^+ $J = 3$–2 line in L483. The velocity intervals are 4.3–5.09 km s^{-1} and 5.7–6.33 km s^{-1} for the peaks and 2.6–4.3 km s^{-1} and 6.33–8.97 km s^{-1} for the lobes. The contour level spacing is 0.2 K km s^{-1} for the blue peak, 0.25 K km s^{-1} for the red peak, 0.2 then 0.1 K km s^{-1} thereafter for the lobes. The black square is the location of the IRAS source. In all plots, the dashed contours are the redshifted peak and the red wing, respectively. The bottom two plots are integrated intensity maps of the red and blue peaks and the blue and red lobes of the HCO^+ $J = 3$–2 line in L1448-C. The velocity intervals are 3.97–4.49 km s^{-1} and 5.16–6.18 km s^{-1} for the peaks and 0.57–3.97 km s^{-1} and 6.18–7.55 km s^{-1} for the lobes. The contour level spacing is 0.3 then 0.1 K km s^{-1} thereafter for the blue peak and red lobe, 0.4 K km s^{-1} for the red peak, 0.2 K km s^{-1} for the blue lobe. The black square is the location of the 2 cm radio continuum source (Curiel et al. 1990).

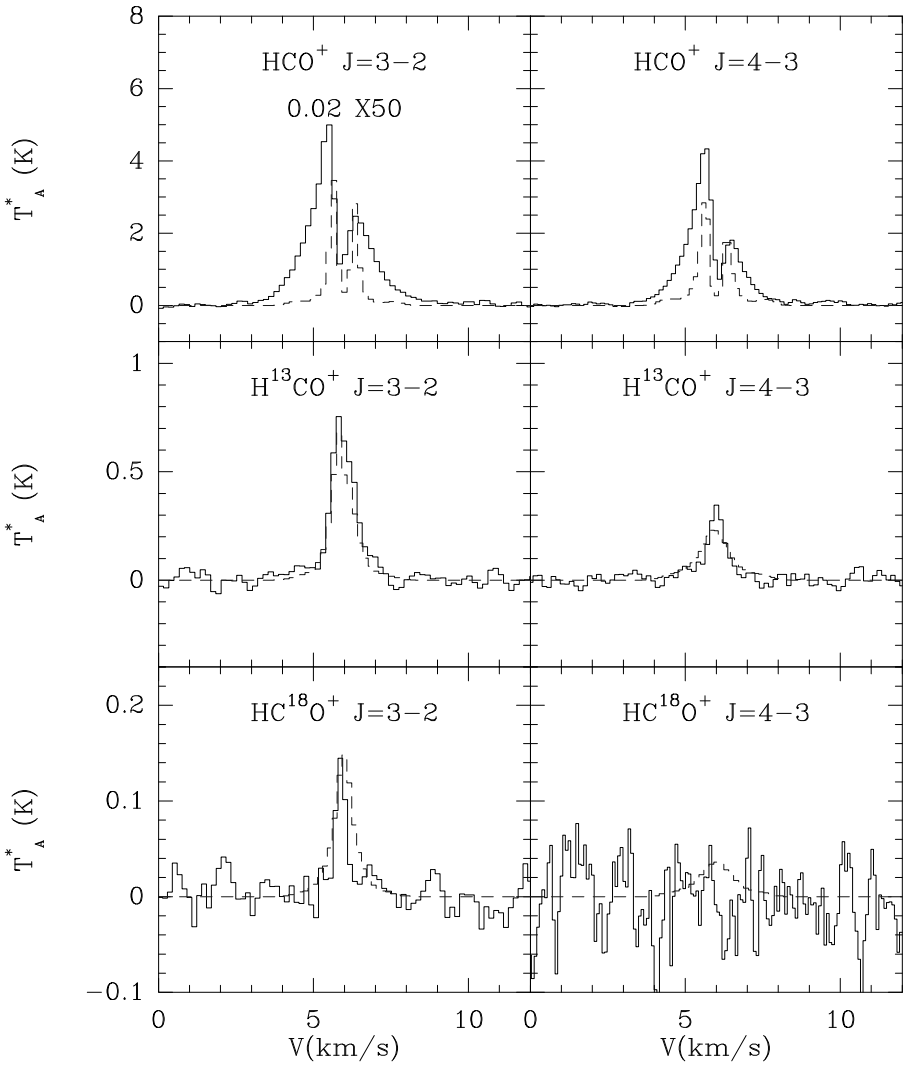

FIG. 16.—The top left-hand panel is the observed HCO^+ $J = 3$–2 line profile (*solid line*) and the simulated line profile (*dashed line*). The infall model has $r_{inf} = 0.026$ pc and $X(HCO^+) = 2.1 \times 10^{-8}$. The vertical lines indicate the velocity intervals used in Fig. 13. The top right-hand panel is the observed HCO^+ $J = 4$–3 line profile (*solid line*) and the simulated line profile (*dashed line*) for the same model. The middle left-hand panel is the observed $H^{13}CO^+$ $J = 3$–2 line profile (*solid line*) and the simulated line profile (*dashed line*). The infall model has $X(H^{13}CO^+) = 4.1 \times 10^{-10}$. The middle right-hand panel is the observed $H^{13}CO^+$ $J = 4$–3 line profile (*solid line*) and the simulated line profile (*dashed line*). The bottom left panel is the observed $HC^{18}O^+$ $J = 3$–2 line profile (*solid line*) and the simulated line profile (*dashed line*). The infall model has $X(HC^{18}O^+) = 7.4 \times 10^{-11}$. The bottom right panel is the observed $HC^{18}O^+$ $J = 4$–3 line profile (*solid line*) and the simulated line profile (*dashed line*).

REFERENCES

Adams, F. C., Lada, C. J., & Shu, F. H. 1987, ApJ, 312, 788
André, P., Martin-Pintado, J., Despois, D., & Montmerle, T. 1990a, A&A, 236, 180
André, P., & Montmerle, T. 1994, ApJ, 420, 837
André, P., Montmerle, T., Feigelson, E. D., & Steppe, H. 1990b, A&A, 240, 321
André, P., Ward-Thompson, D., & Barsony, M. 1993, ApJ, 406, 122
Anglada, G., Estalella, R., Rodriguez, L. F., Torrelles, J. M., Lopez, R., & Canto, J. 1991, ApJ, 376, 615
Anglada, G., Rodriguez, L. F., Torrelles, J. M., Estalella, R., Ho, P. T. P., Canto, J., Lopez, R., & Verdes-Montenegro, L. 1989, ApJ, 341, 208
Avery, L. W., Hayashi, S. S., & White, G. J. 1990, ApJ, 357, 524
Bachiller, R., André, P., & Cabrit, S. 1991, A&A, 241, L43
Bachiller, R., Cernicharo, J., Martin-Pintado, J., Tafalla, M., & Lazareff, B. 1990, A&A, 231, 174
Bachiller, R., Fuente, A., & Tafalla, M. 1995, ApJ, 445, L51
Bally, J., Snell, R. L., & Predmore, R. 1983, ApJ, 272, 154
Barnes, P. J., & Crutcher, R. M. 1990, ApJ, 351, 176
Barsony, M. 1994, in Clouds, Cores, and Low Mass Stars, ed. D. P. Clemens & R. Barvainis (Provo: ASP), 197
Barsony, M., & Chandler, C. J. 1993, ApJ, 406, L71
Barsony, M., Scoville, N. S., Bally, J., & Claussen, M. J. 1989, ApJ, 343, 212
Bontemps, S., André, P., & Ward-Thompson, D. 1995, A&A, 297, 98
Cabrit, S., & André, P. 1991, ApJ, 379, L25
Casali, M. M., Eiroa, C., & Duncan, W. D. 1993, A&A, 275, 195
Chandler, C. J., & Carlstrom, J. E. 1996, ApJ, 466, 388
Chandler, C. J., Gear, W. K., Sandell, G., Hayashi, S., Duncan, W. D., Griffin, M. J., & Hazell, A. S. 1990, MNRAS, 243, 330
Chandler, C. J., & Sargent, A. I. 1993, ApJ, 414, L29
Chen, H., Myers, P. C., Ladd, E. F., & Wood, D. O. S. 1995, ApJ, 445, 377
Chen, H., Tafalla, M., Greene, T. P., Myers, P. C., & Wilner, D. J. 1997, ApJ, 475, L163
Choi, M., Evans, N. J., II, Gregersen, E. M., & Wang, Y. 1995, ApJ, 448, 742
Cohen, M., Harvey, P. M., Schwartz, R. D., & Wilking, B. A. 1984, ApJ, 278, 671
Curiel, S., Raymond, J. C., Rodriguez, L. F., Canto, J., & Moran, J. M. 1990, ApJ, 365, L85
Davidson, J. A. 1987, ApJ, 315, 602
de Geus, E. J., de Zeeuw, P. T., & Lub, J. 1989, A&A, 216, 44
Dent, W. R. F., Matthews, H. E., & Walther, D. M. 1995, MNRAS, 277, 193
Emerson, J. P., Harris, S., Jennings, R. E., Beichman, C. A., Baud, B., Beintema, D. A., Marsden, P. L., & Wesselius, P. R. 1984, ApJ, 278, L49
Fuller, G. A., & Myers, P. C. 1993, ApJ, 418, 273
Fuller, G. A., Lada, E. A., Masson, C. R., & Myers, P. C. 1995, ApJ, 453, 754
Gee, G., Griffin, M. J., Cunningham, C. T., Emerson, J. P., Ade, P. A. R., & Caroff, L. J. 1985, MNRAS, 215, 15P
Gibb, A. G., & Heaton, B. D. 1993, A&A, 276, 511
Goldsmith, P. F., Snell, R. L., Hemeon-Heyer, M., & Langer, W. D. 1984, ApJ, 286, 599
Green, S. 1975, ApJ, 201, 366
Harvey, P. M., Wilking, B. A., & Joy, M. 1984, ApJ, 278, 156
Hurt, R. L., & Barsony, M. 1996, ApJ, 460, L45
Hurt, R. L., Barsony, M., & Wootten, A. 1996, ApJ, 456, 686
Jennings, R. E., Cameron, D. H. M., Cudlip, W., & Hirst, C. J. 1987, MNRAS, 226, 461
Johnston, K. J., Sloanaker, R. M., & Bologna, J. M. 1973, ApJ, 182, 67
Keene, J., Davidson, J. A., Harper, D. A., Hildebrand, R. H., Jaffe, D. T., Loewenstein, R. F., Low, F. J., & Pernic, R. 1983, ApJ, 274, L43
Lada, C. J. 1987, in Star Forming Regions, ed. M. Peimbert & J. Jugaku (Dordrecht: Reidel), 1
Lada, C. J., & Wilking, B. A. 1984, ApJ, 287, 610
Ladd, E. F., Adams, F. C., Casey, S., Davidson, J. A., Fuller, G. A., Harper, D. A., Myers, P. C., & Padman, R. 1991, ApJ, 366, 203
Lay, O. P., Carlstrom, J. E., & Hills, R. E. 1995, ApJ, 452, L73
Leung, C. M., & Brown, R. L. 1977, ApJ, 214, L73
Lis, D. C., Carlstrom, J. E., & Phillips, T. G. 1991, ApJ, 370, 583
Mardones, D., Myers, P., Caselli, P., & Fuller, G. 1994, in Clouds, Cores, and Low Mass Stars, ed. D. P. Clemens & R. Barvainis (Provo: ASP), 192
McMullin, J. P., Mundy, L. G., Wilking, B. A., Hezel, T., & Blake, G. A. 1994, ApJ, 424, 222
Menten, K. M., Serabyn, E., Gusten, R., & Wilson, T. L. 1987, A&A, 177, L57
Mezger, P. G., Chini, R., Kreysa, E., Wink, J. E., & Salter, C. J. 1988, A&A, 191, 44
Mezger, P. G., Sievers, A. W., Haslam, C. G. T., Kreysa, E., Lemke, R., Mauersberger, R., & Wilson, T. L. 1992, A&A, 256, 631
Monteiro, T. S. 1985, MNRAS, 214, 419
Moriarty-Schieven, G. H., Butner, H. M., & Wannier, P. G. 1995a, ApJ, 445, L55
Moriarty-Schieven, G. H., Wannier, P. G., Magnum, J. G., Tamura, M., & Olmsted, V. K. 1995b, ApJ, 455, 190
Mundy, L. G., Wilking, B. A., & Myers, S. T. 1986, ApJ, 311, L75
Myers, P. C., Bachiller, R., Caselli, P., Fuller, G. A., Mardones, D., Tafalla, M., & Wilner, D. J. 1995, ApJ, 449, L65
Myers, P. C., & Ladd, E. F. 1993, ApJ, 413, L47
Parker, N. D., Padman, R., & Scott, P. F. 1991, MNRAS, 252, 442
Persi, P., Ferrari-Toniolo, M., Busso, M., Origlia, L., Robberto, M., Scaltriti, F., & Silvestro, G. 1990, AJ, 99, 303
Persi, P., Ferrari-Toniolo, M., Marenzi, A. R., Anglada, G., Chini, R., Krugel, E., & Sepulveda, I. 1994, A&A, 282, 233
Rawlings, J. M. C., Harquist, T. W., Menten, K. M., & Williams, D. A. 1992, MNRAS, 255, 471
Richer, J. S. 1990, MNRAS, 245, 24P
Richer, J. S., Hills, R. E., & Padman, R. 1992, MNRAS, 254, 525
Richer, J. S., Padman, R., Ward-Thompson, D., Hills, R. E., & Harris, A. I. 1993, MNRAS, 262, 839
Sandell, G., Aspin, C., Duncan, W. D., Russell, A. P. G., & Robson, E. I. 1991, ApJ, 376, L17
Shu, F. H. 1977, ApJ, 214, 488
Stutzki, J., Ungerechts, H., & Winnewisser, G. 1982, A&A, 111, 201
Tafalla, M., & Bachiller, R. 1995, ApJ, 443, L37
Umemoto, T., Iwata, T., Fukui, Y., Mikami, H., Yamamoto, S., Kameya, O., & Hirano, N. 1992, ApJ, 392, L83
van Dishoeck, E. F., Blake, G. A., Jansen, D. J., & Groesbeck, T. D. 1995, ApJ, 447, 760
Velusamy, T., Kuiper, T. B. H., & Langer, W. D. 1996, ApJ, 451, L75
Walker, C. K., Adams, F. C., & Lada, C. J. 1990, ApJ, 349, 515
Walker, C. K., Lada, C. J., Young, E. T., Maloney, P. R., & Wilking, B. A. 1986, ApJ, 309, L47
Wilking, B. A., Claussen, M. J., Benson, P. J., Myers, P. C., Terebey, S., & Wootten, A. 1994, ApJ, 431, L119
Wilking, B. A., Lada, C. J., & Young, E. T. 1989a, ApJ, 340, 823
Wilking, B. A., Mundy, L. G., Blackwell, J. H., & Howe, J. E. 1989b, ApJ, 345, 257
Wilson, T. L., Mehringer, D. M., & Dickel, H. R. 1995, A&A, 303, 840
Wootten, A. 1989, ApJ, 337, 858
Zhou, S. 1992, ApJ, 394, 204
———. 1995, ApJ, 442, 685
Zhou, S., Evans, N. J., II, Butner, H. M., Kutner, M. L., Leung, C. M., & Mundy, L. G. 1990, ApJ, 363, 168
Zhou, S., Evans, N. J., II, Kompe, C., & Walmsley, C. M. 1993, ApJ, 404, 232
Zhou, S., Evans, N. J., II, & Wang, Y. 1996, ApJ, 466, 296
Zhou, S., Evans, N. J., II, Wang, Y., Peng, R., & Lo, K. Y. 1994, ApJ, 433, 131
Zinnecker, H., Bastien, P., Arcoragi, J.-P., & Yorke, H. W. 1992, A&A, 265, 726